Revision 1

Synthesis, characterization and thermodynamics of arsenates forming in the Ca-Fe(III)-As(V)-NO_3 system: Implications for the stability of Ca-Fe arsenates

DOGAN PAKTUNC[1,2,*], JURAJ MAJZLAN[3], ARTIS HUANG[2], YVES THIBAULT[1], MICHEL B. JOHNSON[4], MARY ANNE WHITE[4]

[1]CanmetMINING, 555 Booth Street, Ottawa, ON, K1A 0G1 Canada, [2]Department of Earth Sciences, University of Ottawa, Ottawa, ON, K1N 6N5 Canada, [3]Institute of Geosciences, Burgweg 11, Friedrich-Schiller University, D-07749 Jena, Germany, [4]Department of Chemistry and Institute for Research in Materials, Dalhousie University, Halifax, NS, B3H 4R2, Canada

* *Corresponding author*
T: 613-947-7061
F: 613-996-9673
dpaktunc@uOttawa.ca

ABSTRACT

Arseniosiderite and yukonite are among the important arsenate minerals occurring as secondary alteration products in relation to the oxidation of arsenopyrite and arsenian pyrite and as discrete grains in some gold ores, mine tailings, and contaminated soils. Characteristics of these Ca-Fe arsenate species are not well known and our understanding of the conditions promoting their formation and dissolution is limited. Long- and short-range structural characteristics and thermodynamic properties of the Ca-Fe arsenates forming in the Ca-Fe(III)-As(V)-NO_3 system were determined to better predict the mineralogical transformations taking place in neutralized sludge and tailings environments, and their influence on arsenic mobilization. Yukonite and arseniosiderite readily form from solutions with highly variable compositions at a wide pH range from slightly acidic to alkaline conditions. Calcium concentrations corresponding to molar Ca/(Ca+Fe+As) ratios as low as 0.1 appear to be adequate for their formation. Our experimental results confirm observations in natural settings and mine tailings where scorodite is progressively replaced by yukonite and arseniosiderite. The initial amorphous precipitates made of small oligomeric units of edge-sharing FeO_6 octahedra with bridging arsenate evolve to yukonite through the establishment of corner linkages between the FeO_6 chains. Yukonite represents a nanocrystalline precursor and Ca-deficient variety of arseniosiderite. Formation of arseniosiderite is kinetically controlled with faster development of crystallinity at neutral to slightly acidic pH and slower kinetics under alkaline conditions. Calorimetric measurements provided an enthalpy of formation value of –1950.3±3.1 $kJmol^{-1}$ and standard entropy of 237.4±4.4 $Jmol^{-1}K^{-1}$ for arseniosiderite [with composition $Ca_{0.663}Fe_{1.093}(AsO_4)(OH)_{1.605}{\cdot}0.827H_2O$], the corresponding Gibbs free energy of formation is –1733±3.4 $kJmol^{-1}$. A rough estimate of the thermodynamic properties of yukonite is also provided. Arseniosiderite is a stable arsenate between pH 3.5 and 7.5 in solutions saturated with respect to soluble Ca minerals such as calcite, gypsum, anorthite or Ca-montmorillonite. Arsenic release from mine wastes and contaminated soils can be effectively controlled by arseniosiderite and the conditions promoting its formation such as lime-treatment leading to gypsum saturation in ferric arsenate solutions would prove to be desirable for stabilizing arsenic in the form of arseniosiderite in mine wastes.

Keywords: arsenic, arsenate, arseniosiderite, yukonite, arsenic control, mine wastes

INTRODUCTION

Ca-Fe arsenates such as yukonite and arseniosiderite are important constituents of mine wastes resulting from the processing of some gold and base metal ores and neutralization of acidic mine effluents (Paktunc et al. 2004). Cyanide leaching of gold ores under highly alkaline conditions with the use of lime promotes the formation of Ca-Fe arsenates from Fe- and As-rich process solutions. Calcium, which is widely available in some process solutions, appears to increase the solubility of ferric arsenate compounds (Swash and Monhemius 1995) and it has a detrimental effect on arsenic stabilization because of the co-precipitation of arseniosiderite-like oligomeric units during adsorption of As on goethite (Paktunc et al. 2004). Disposal and immobilization of arsenic in the form of Ca arsenate compounds in mine and industrial wastes was deemed to be inappropriate due to their high solubilities (Robins and Tozawa 1982). Arseniosiderite and yukonite were reported in gold ores and mine tailings occurring as secondary alteration products after arsenopyrite, arsenian pyrite, or arsenate minerals such as scorodite (Paktunc et al. 2003, 2004). Ca-Fe arsenates were also reported in naturally contaminated soils at the Mokrsko-west gold deposit (Filippi et al. 2007; Drahota et al. 2009), impacted soil near an industrial site in France (Cances et al. 2008), mine tailings and contaminated soils at several abandoned gold mine sites in Nova Scotia (Walker et al. 2009), mine wastes in the Mojave desert (Kim et al. 2012) and historic gold mine wastes at Empire Mine State Historic Site, California (Burlak 2012). Arseniosiderite was also inferred to be present in mine tailings at the Lava Cap mine, Nevada (Foster et al. 2011). Yukonite was first reported in a mine claim near Tagish Lake, Yukon, Canada by Tyrrell and Graham (1913). Other reported occurrences include Sterling Hill mine, New Jersey, USA (Dunn 1982), Saalfeld, Thüringen, Germany (Ross and Post 1997), dolomitic limestones of Redziny, Poland (Pieczka et al. 1998), Nalychevskie hot springs, Russia (Nishikawa et al. 2006) and mineralized karstic cave, Cosenza, Italy (Garavelli et al. 2009). Arseniosiderite belongs to the mitridatite (Moore and Araki 1976) and robertsite structural group of minerals which can be characterized by the general formula $Ca_2A_3O_2(TO_4)_3{\cdot}nH_2O$ with A=Fe, Mn; T=As, P and n=2 or 3 (Andrade et al. 2012).

Crystal structure of yukonite is not known. As summarized by Garavelli et al. (2009), the reported compositions of yukonite are variable.

Solubilities of arseniosiderite and yukonite are not known although they are considered to be relatively soluble based on cursory leaching and limited solubility tests (e.g. Krause and Ettel 1989; Swash and Monhemius 1994). Despite the common occurrences of Ca-Fe arsenates in a variety of settings, our understanding of the characteristics of the Ca-Fe arsenate phases species is limited and the conditions promoting their formation and stabilities are not well known. In addition, it is not known how ferric arsenates and arsenical ferrihydrite behave when in contact with Ca-rich solutions. These gaps impose significant limitations to our ability to predict the long-term behavior of arsenic in mine wastes and impacted soil.

To fulfill these needs, we carried out an experimental study in the Ca-Fe(III)-As(V)-NO_3 system to determine the controls on the formation and transformation of Ca-Fe arsenates under slightly acidic to alkaline conditions and their structural and thermodynamic properties. This study forms an extension to the Fe-AsO_4 and Fe-AsO_4-SO_4 systems we studied (Paktunc et al. 2008, 2013). In addition, we report new mineralogical findings from a paleo-weathered gold deposit, which would serve as a natural analog of mineralogical transformations for the long-term prediction of arsenic mobilization from mine wastes.

MATERIALS AND METHODS

Synthesis experiments

The syntheses were performed in batch and continuous modes. The batch mode experiments were performed at 75-85 ºC and pH 4-10.6 from solutions with variable molar ratios of $Ca(NO_3)_2$, $Fe(NO_3)_3 \cdot 9H_2O$ and Na_2HAsO_4 in reaction vessels sealed with rubber stoppers and Parafilm® to reduce vapor loss. The reagents were mixed at room temperature prior to their placement in reaction vessels with heating mantles or in silicone oil baths equipped with heating and cooling elements to maintain a constant solution temperature. The solutions, initially transparent with a light yellow tint at room temperature, darkened to a reddish color at synthesis temperature but maintained their

transparency. The solutions were continuously stirred by Teflon impellers at 200 rpm and the pH adjustments were made by HNO_3 and NaOH. Visible polymerization occurred only after the addition of NaOH. Slurry samples were collected at various time intervals by inserting Nalgene tubes and 50 mL syringes. The duration of the syntheses ranged from 4 to 35 days. The continuous mode experiments were performed at 85 ºC and pH 4.5, 8.5 and 9 from 0.2 M $Ca(NO_3)_2$, 0.3 M $Fe(NO_3)_3 \cdot 9H_2O$ and 0.3 M Na_2HAsO_4 stock solutions. The 2-L reaction vessels were placed in heating mantle units with thermocouple. The feed solution was pumped to the reaction vessel at 12 mL/min and the overflow was pumped from the vessel at the same speed while the solution in the reactor was mixed at 200 rpm by a Teflon impeller. The solution pH was maintained by an autotitrator. The experiments at pH 4.5 and 8.5 were conducted for 20 days whereas the one at pH 9 was for 33 days. The pH 9 experiment was sampled at 12-hour intervals by collecting the overflow into a clean flask.

Slurry samples of 25 to 100 mL were centrifuged and washed three times with deionized water. Following this, the precipitates were freeze-dried or air-dried at room temperature.

Calorimetric experiments

Chemical composition of the arseniosiderite sample was measured by inductively coupled plasma optical emission spectrometry after dissolution of a known mass of the sample in 5 mL of ultrapure HNO_3 and 5 mL of deionized water. Water content was determined by thermogravimetry (TG), by heating the sample in a stream of air from room temperature to 600 °C with a heating rate of 10 ºC/min.

For the solution calorimetric experiments at 25 ºC, we used a commercial IMC-4400 isothermal microcalorimeter (Calorimetry Sciences Corporation) which we modified for the purposes of acid-solution calorimetry. The liquid bath of the calorimeter was held at a constant temperature of 298.15 K with fluctuations smaller than 0.0005 K. The calorimetric solvent was 25 g of deionised water or 25 g of 5 M HCl contained in a polyetheretherketone (PEEK) cup with a total volume of 60 mL. The cup was then closed with a PEEK screwable lid and inserted into the calorimeter well. The calorimeter stabilized after ~8 hours. During the stabilization and the experiment, the solvent was

stirred using a SiO_2 glass stirrer by a motor positioned about 40 cm from the active zone of the instrument. The sample was pressed into a pellet and weighed with a micro-balance. The pellet was then dropped through a SiO_2 glass tube into the solvent and the heat produced or consumed during the dissolution was measured. The heat flow between the reaction cup and the constant temperature reservoir was then integrated to calculate the caloric effect. A typical experiment lasted 50-60 minutes and the end of the experiment was judged from the return of the baseline to the pre-experiment position. The pellet mass was calculated according to the stoichiometry of the thermochemical cycle, relative to 2.00 mg of KCl. The calculated mass of the arseniosiderite pellets was 6.71 mg whereas its actual mass was 6.95±0.05 mg. The calorimeter was calibrated by dissolving ~20 mg pellets of KCl in 25 g of deionised water. Prior to each calibration measurement, KCl was heated overnight in a furnace at 800 K to remove the adsorbed water. The expected heat effect for the calibration runs was calculated from Parker (1965).

Heat capacity was measured by relaxation calorimetry using a commercial Physical Property Measurement System (PPMS, from Quantum Design, San Diego). With due care, accuracy can be within 1% for 5 K to 300 K, and 5% for 0.7 K to 5 K (Kennedy et al., 2007). Due to the hydrated nature of the mineral sample, it needed to be isolated from the vacuum required for heat capacity measurements. To achieve this, the aluminum DSC pan method by Marriott et al. (2006) was employed. This method requires four heat capacity runs to obtain the sample heat capacity: (1) an addendum measurement of the platform with a thin layer of grease, (2) the DSC pan with ca. 3 mg Apiezon® N grease within the pan and the lid resting inside but not sealed, (3) an addendum measurement of the platform with a thin layer of grease, and (4) the hermetically sealed DSC pan with the sample embedded in the internal grease. Measurements (1) and (2) give the heat capacity of the pan and internal grease and the measurements (3) and (4) give the heat capacity of the pan+sample+internal grease. Step (3) was required because it was not possible to carry out (2) and (4) with the precisely same amount of grease on the platform. The results of ((4)-(2)) – ((2)-(1)) give the sample heat capacity. The heat capacity of run (2) is subtracted from run (4), giving the sample heat capacity. Measurements were conducted in the temperature interval 0.4 to 300 K. The sample was pressed into pellets

using a stainless steel die with a diameter of 7/64". A Carver Model 3912 press provided an applied force of 750 lbs, resulting in a pressure of 0.55 GPa on the pellets. The mass of the two arseniosiderite pellets, weighed using a semi-microbalance, were 8.69±0.02 mg and 7.11±0.02 mg.

Natural occurrences

Two mineral specimens were obtained from the British Museum, Natural History (Department of Mineralogy). The specimens, labeled "arseniosiderite (var. yukonite) (ott BM 1916, 454) Daulton mine, Yukon, Canada" and "arseniosiderite, (ott BM 1974, 371) Las Animas, Sonora, Mexico" were tiny mineral grains. Portions of the mineral grains were mounted in epoxy and polished.

Rock samples were collected from several outcrops representing the transition zone between the sulfide and oxide ore bodies at the Ketza River gold mine in Yukon. The samples were characterized on cold-epoxy mounts having a 25 to 30 mm diameter and a thickness of approximately 10 mm. The epoxy mounts were polished using oil-based diamond suspension to prevent degradation of the water-soluble phases.

Characterization

Following their digestion in sealed vessels under microwave heating, the precipitates were analyzed for Ca, Fe, As, Na and Si by inductively coupled plasma atomic emission spectrometry.

X-ray diffraction analyses were performed using a Rigaku D/MAX 2500 rotating anode X-ray powder diffractometer using Cu Kα radiation at 50 kV, 260 mA, step-scan 0.02^{o}, scan rate at 1^{o} per minute in 2θ. The samples were finely ground in a mortar and pestle, and placed on zero-background plates and dispersed by acetone or packed on Teflon covered aluminum sample holders for the X-ray powder diffraction analysis.

Structural information for individual phases was obtained directly on the polished sections using a Rigaku Rapid II microfocus rotating anode X-ray diffractometer configured with confocal multilayer X-ray optic. Cr Kα X-rays were generated at an accelerating voltage of 35 kV with a current of 25 mA. The incident X-ray beam was then focused and collimated down to 30 μm on the sample. The diffraction images were

recorded on a large aperture curved image plate. The angle (χ) between the sample surface and the X-ray beam axis was kept fixed at 45°. However, to improve random crystallographic orientation of the phase(s) investigated with respect to the incident X-rays, the polished section was rotated along an axis normal to its surface (□) and oscillated around an axis perpendicular to the X-ray beam (ω). Conventional intensity vs. 2θ patterns were constructed using the 2DP Rigaku software through integration of the intensity along the rings of the diffraction images. Phase identification was made with the JADE software (v. 9.0) interfaced with the ICDD database.

Electron microprobe analyses (EPMA) were performed by a JEOL733 and JEOL JXA 8900 using wavelength dispersive spectrometers (WDS) operating at 15 and 20 kV with a beam current of 15, 20 and 30 nA and counting times of 10 to 40 seconds. The following X-ray lines and standards were used: Fe Kα (synthetic Fe_2O_3), Zn Kα (synthetic ZnO), Mn Kα (synthetic $MnTiO_3$), Ca Kα (sphene, wollastonite), Mg Kα and Al Kα (synthetic $MgAl_2O_4$), As Kα (synthetic InAs, $FeAs_2$), Si Kα (wollastonite), K Kα (orthoclase), Na Kα (synthetic $NaNbO_3$), S Kα (synthetic $PbSO_4$, FeS_2, $BaSO_4$) and P Kα (apatite). The S Kα peak was scanned on each phase analyzed to track potential shift. Matrix corrections were made using the □*(ρz)* program provided by JEOL. Characteristic X-ray intensities were monitored as a function of time to determine optimal current density conditions (probe current, beam size) in order to avoid potential beam damage artifacts (e.g. Dunn, 1982). We noticed that the natural nanocrystalline aggregates of Ca-Fe arsenates had high nanoporosity allowing epoxy to impregnate at the scale of the excitation volume during EPMA analyses. The epoxy contribution to the analyses resulted in low totals, but the relative proportion of the cations should not be affected.

X-ray Absorption Fine Structure (XAFS) spectroscopy experiments were carried out at the PNC-CAT bending magnet beamline of the Advanced Photon Source, Argonne, Illinois, USA. The samples were prepared separately for As K-edge and Fe K-edge XAFS by mixing with boron nitride to achieve a sample thickness of about 1 absorption length. The XAFS spectra were collected at room temperature in both the transmission and fluorescence modes. Several samples were analysed at -183 °C at an extended *k* range of 16 $Å^{-1}$. Each sample was scanned six times. Data reduction and analysis were accomplished by ATHENA/ARTEMIS/IFEFFIT (Ravel and Newville 2005). XAFS data

247 analysis considered the theoretical phase and amplitude functions generated in FEFF6
248 (Rehr et al. 1991).
249 Transmission electron microscopy (TEM) samples were prepared by placing a drop of
250 sonicated dilute precipitate in ethanol onto a Lacey Carbon Film on a copper TEM grid.
251 Examinations were performed using a Philips CM20-FEG operated at 197 keV
252 (CANMET), a JEOL JEM2100 field emission TEM operated at 200 keV (University of
253 Ottawa) and a FEI TITAN operated at 300 keV (McMaster University). The FEI TITAN
254 microscope is equipped with a CEOS hexapole image Cs corrector and a Gatan Ultrascan
255 CCD camera. Semi-quantitative microanalyses of Ca, Fe and As were performed using an
256 Oxford Instruments thin-window energy-dispersive X-ray spectrometer with an INCA
257 system analyzer or a Link (Oxford) PentaFET energy dispersive X-ray spectrometer.
258
259 **RESULTS**
260
261 **Yukonite and arseniosiderite specimens**
262 X-ray diffraction analysis of the mineral grains confirmed their identities as yukonite
263 (PDF 45-1358) for the arseniosiderite (var. yukonite) specimen from the Daulton Mine,
264 Yukon, Canada and arseniosiderite (PDF 26-1002) for the arseniosiderite specimen from
265 Las Animas, Sonora, Mexico. The arseniosiderite specimen consists of fibrous
266 aggregates. Electron microprobe analyses indicate that the individual particles are
267 homogeneous. The average composition of the arseniosiderite specimen is 14.77 wt%
268 CaO, 31.74 wt% Fe_2O_3, 36.95 wt% As_2O_5, 3.63 wt% SiO_2, 0.25 wt% MnO and 0.11 wt%
269 Na_2O, based on 30 spot microanalyses on 10 mineral grains (Table 1). The corresponding
270 mineral formula is $Ca_2Fe_3(AsO_4)_{2.4}(SiO_4)_{0.5}(OH)_{3.9}\cdot 3.3H_2O$ with H partitioned between
271 OH and H_2O to maintain charge balance. This composition is comparable to the average
272 of that for arseniosiderite from the Ketza River mine based on 42 arseniosiderite grains
273 (Paktunc et al. 2004) which is $Ca_2Fe_3(AsO_4)_{2.8}(OH)_{4.3}\cdot 2.6H_2O$ and to the nominal
274 arseniosiderite composition, $Ca_2Fe_3(AsO_4)_3O_2\cdot 3H_2O$. Electron microprobe analyses of
275 arseniosiderite reported by Filippi et al. (2007) and Gomez et al. (2010), recast as
276 $Ca_{1.9}Fe_3(AsO_4)_{2.7}(SiO_4)_{0.1}(OH)_{4.2}\cdot 4H_2O$ for the Mokrsko west gold deposit and as
277 $Ca_2Fe_3(AsO_4)_{2.5}(OH)_{5.7}\cdot 4.8H_2O$ for the arseniosiderite specimen from Romaneche,

France, are also comparable. These formula calculations assume the presence of OH^- instead of O^{2-} in the arseniosiderite structure as per Gomez et al. (2010).

The yukonite specimen from the Daulton Mine has slightly variable composition with 11.56±1.31 wt% CaO, 36.05±4.64 wt% Fe_2O_3, 37.15±3.90 wt% As_2O_5, 0.40±0.15 wt% SiO_2, 0.34±0.07 wt% MnO, 0.13±0.04 wt% Na_2O and 0.17±0.07 wt% K_2O, based on 15 spot microanalyses (Table 1). Its average mineral formula can be defined as $Ca_{1.4}Fe_3(AsO_4)_{2.1}(OH)_{5.1}\cdot 2.2H_2O$. This composition is similar to those of the yukonite specimens reported by Ross and Post (1997) from Tagish Lake and Jambor#16 as reported by Dunn (1982). The average composition of yukonite from the Ketza River mine (Paktunc et al. 2004) which is $Ca_{1.5}Fe_3(AsO_4)_{2.3}(SiO_4)_{0.1}OH)_{4.6}\cdot 4.4H_2O$ is also similar. With the recalculated composition of $Ca_{1.8}Fe_3(AsO_4)_{2.5}(SiO_4)_{0.3}OH)_{3.8}\cdot 3.8H_2O$, yukonite from the Grotta Della Monaca cave in Italy (Garavelli et al. 2009) appears to be slightly less deficient in Ca and As.

Batch synthesis

A summary of the batch synthesis experiments is provided in Table 2. Representative examples of the X-ray diffraction patterns of the intermediary and final precipitates are given in Figure 1.

The initial precipitates are X-ray amorphous and characterized by two broad humps centered at about 30º and 60º (2θ Cu Kα) similar to the amorphous ferric arsenate described by Paktunc et al. (2008). It seems that the main hump gradually moves to higher 2θ with increased pH (i.e. 30.0º at pH 6, 30.5º at pH 7, 30.8º at pH 8 and 31.1º at pH 9). The shift of the main hump to higher 2θ values was attributed to the formation of ferrihydrite in the Ca-free amorphous ferric arsenate precipitates with Fe/As molar ratios of 2 and greater (Paktunc et al. 2008). The chemical compositions of the initial precipitates are similar to yukonite and arseniosiderite (Table 3).

After about 13 h at pH 6 to 8 and 37 h at pH 9, peaks at 2θ (Cu-Kα) values of 15.5º, 27.0º, 31.9º, 40.2º, 51.6º and 55.8º corresponding to yukonite (PDF 45-1358 and 51-1416) and arseniosiderite (PDF 26-1002) appear (Fig. 1). The low-angle yukonite peak at 6.3º (14 Å) and arseniosiderite peak at 10.1º (8.8 Å) are absent. With continued synthesis after about 24 h at pH 6 to 8, a low-angle peak at ~9º (10 Å) appears. This probably

corresponds to the arseniosiderite peak at 10.0º (8.83 Å). The low-angle peak at ~8.8º which develops as a hump at 24 h appears to move towards smaller *d*-spacings with increased synthesis as the diffraction maximum becomes more prominent (Fig. 1). The changes in the *d*-spacings with time are exponential for all the precipitates at pH 6, 7 and 8 (Fig. 2). In addition, humps develop with synthesis time at ~19º and both shoulders of the main reflection at ~32º corresponding to the arseniosiderite peaks of 4.7, 2.9 and 2.6 Å. The peaks gradually sharpen with time. The low-angle peak develops as a hump beginning at about 24 h at pH≤8. It is absent in the precipitates formed at pH 9 with the exception of the subtle hump at 94 and 286 h. It appears that arseniosiderite forms at a wide pH range but its formation is kinetically controlled. The low angle arseniosiderite peak moves to a slightly lower *d*-spacing (i.e. 9.25 Å) at pH 8 as opposed to ~10 Å at pH 6 and 7 (Fig. 2).

The end products of synthesis after 288 h from solutions containing 1M of Ca, Fe and As are scorodite at pH 4, scorodite and arseniosiderite at pH 5 and arseniosiderite at pH 6. The solution compositions of 2M Ca, 3M Fe and 3M As produced scorodite and arseniosiderite at pH 5, and arseniosiderite at pH 6 and 7, all after 480 hours of synthesis. The arseniosiderite precipitates have the following compositions: $Ca_{1.8}Fe_3(AsO_4)_{2.9}(SiO_4)_{0.1}(OH)_{4.6}\cdot 6.6H_2O$ and $Ca_{1.5}Fe_3(AsO_4)_{2.3}(SiO_4)_{0.7}(OH)_{3.3}\cdot 6.7H_2O$ whereas yukonite is $Ca_{1.7}Fe_3(AsO_4)_{2.3}(SiO_4)_{0.7}(OH)_{3.5}\cdot 5.9H_2O$ (Table 3). Silicon concentrations resulted from etching of the Pyrex (borosilicate) reactor especially at high pH and under prolonged reaction conditions are assumed to be structural because they make up the deficiencies in the As analyses with the exception of a yukonite precipitate. This assumption is supported by scanning electron microscope/microprobe examinations at sub-micrometer spatial resolutions. The initial amorphous precipitates possess similar compositions to their crystalline counterparts (Table 3). Formation of Ca arsenates including johnbaumite, the calcium arsenate member of the apatite family (Dunn et al. 1980) and an unknown compound restricted to starting pH of 8.5-10 and initial solution Ca/(Ca+Fe) ratios of 0.67 and greater. The unknown precipitate is characterized by the two dominant peaks at *d*-spacings of 6.65 and 3.31 Å, and by minor peaks at 5.35, 4.80, 4.52, 3.36, 3.14, 2.95, 2.58 and 1.65 Å. The precipitate has the following structural formula: $Ca_3(AsO_4)_2\cdot 2.3H_2O$ (Table 3). Higher Fe concentrations (i.e.

Fe/(Ca+Fe+As)>0.6) promote the formation of ferrihydrite. Scorodite forms at pH 4 and less.

Continuous synthesis

During the continuous synthesis experiments at pH 9, yukonite formed after 48 h and a Ca arsenate appeared after 144 h (Table 2). The end product after 480 hours of continuous synthesis is yukonite at pH 8.5 and arseniosiderite at pH 4.5 (Fig. 3). The low-angle peak at 9.7 Å is absent in the precipitates formed during continuous synthesis at pH 8.5 and 9. Yukonite formed at pH 9 appears to be less crystalline than that formed at pH 8.5. Continuous synthesis experiments performed at pH 9 produced an unknown Ca arsenate after about 144 hours. Powder XRD patterns and chemical analyses ($Ca_3(AsO_4)_2 \cdot 2.3H_2O$) indicate that it is the same compound formed during the batch synthesis experiments from solutions with initial Ca/(Ca+Fe)≥0.67. Chemical composition of the arseniosiderite end product resulting from continuous synthesis at pH 4.5, $Ca_{1.9}Fe_3(AsO_4)_{2.8}(SiO_4)_{0.1}(OH)_{4.1} \cdot 2.4H_2O$ (Table 3) is similar to the arseniosiderite specimens reported in Table 1. The yukonite final precipitate formed at pH 8.6 after 480 hours has a Si concentration that is too high to be structural (Table 3). It appears that this precipitate has an amorphous SiO_2 likely to have originated from the Pyrex glass reactor under prolonged reaction conditions as described earlier.

TEM characterization

The initial precipitates are large lumpy agglomerations of smaller particles (Fig. S1). Selected area electron diffraction patterns (Fig. S2) and the absence of internal structures at high-resolution images (Fig. 4) suggest that the initial precipitates are largely amorphous. Particles have uniform chemical composition (Fig. S1). The precipitates formed at 24 h are nanocrystalline yukonite particles measuring on average 5 nm × 15 nm (Fig. 5). The grains are lath-shaped and characterized by the presence of prominent lattice fringes developed along the longer dimensions of the laths. There are 4 to 6 such lattice fringes in individual grains with spacing of about 9.5 to 10.3 Å (Fig. S3 and S4). Fast Fourier transforms of the high-resolution TEM (HRTEM) images indicate that the *d*-spacings are in the 9.1-10.5 Å range (Fig. S3). Other sets of lattice fringes have *d*-

spacings of 2.7-2.9, 3.1-3.2, 3.6, 4.2-4.8 and 5.6-5.8 Å. Semi-quantitative microanalyses of the precipitates suggest a chemical similarity to yukonite in terms of atomic proportions of Fe, Ca and As (Table S1). Dark fringes probably represent the FeO_6 octahedral layers sandwiched between arsenate tetrahedra (Fig. 5d; Fig. S4) corresponding to (100) of arseniosiderite (8.84 Å). Some of these octahedral layers are very long reaching to about 50 nm in length with wavy or curvy appearance (Fig. 5a,b,c,d). The wavy nature of the octahedral layers is probably due to the arsenate site vacancies linking pseudo-trigonal rings and Ca vacancies, which would cause weak interlayer interactions.

Extended X-ray absorption fine structure spectroscopy (EXAFS)

Both the As K-edge and Fe K-edge spectra of the initial precipitates are broadly similar (Fig. 6-9). The changes in the spectra with synthesis time are gradual, indicating that the local structures around the As and Fe atoms in the precipitates evolve with time. For instance, the oscillation feature at ~6.8 $Å^{-1}$ of the As K-edge spectra becomes prominent in the final precipitates forming after 286 hours (Fig. 6). The Fe K-edge spectra display oscillation features developing at ~7.4, 9.5, 10.5 and 11 $Å^{-1}$ with synthesis time suggesting increased contributions from more distant neighbor atoms (Fig. 8). The final precipitates have broadly similar Fe-EXAFS spectra especially at less than ~9 $Å^{-1}$ but subtle differences appear at > ~9 $Å^{-1}$ between those formed at pH 7 and 8 and those formed at pH 4.5 and 6. The differences are reflected in their Fourier transforms with the lower pH precipitates having slightly higher magnitudes at ~3.2 Å in comparison to the peak at ~2.7 Å (distances uncorrected for phase shift).

Fitting of the As K-edge spectra indicates that the As-O radial distances are relatively uniform at 1.69-1.70 Å (Table 4) with the average of 9 samples being 1.694±0.05 Å. The As K-edge spectra of the initial precipitates were fitted with an Fe shell with 2 Fe atoms with As-Fe distances ranging from 3.29±0.04 to 3.32±0.03 Å. The intermediary precipitates formed at 24, 37 and 49 hours and the final precipitates possess two Fe shells, one with 2 Fe at a distance between 3.19±0.02 and 3.21±0.02 Å, and another with 1 Fe between 3.34±0.07 and 3.35±0.05 Å. Successive inclusion of the multiple scattering paths As-O1-O2, As-O1-As-O2, As-O1-As-O1 and As-O-Fe designated as MS21, MS31,

MS32 and MS22 (Manceau et al. 2007) resulted in the improvement of the fit quality only with MS21, although MS31 and MS32 enhanced the fit over the first oscillation feature at ~5 $Å^{-1}$.

Uniform radial Fe-O distances at 1.99±0.00 Å characterize the initial precipitates (Table 5). The Fe K-edge spectra of the initial precipitates can be simulated with 1.5 Fe at ~3.04 Å, 2 As at ~3.34 Å and 0.5 Ca at 3.67 Å. The fit quality is improved with the inclusion of multiple scattering paths originating from within FeO_6 octahedra including Fe-O-O (triangular), Fe-O-O (collinear) and Fe-O-Fe-O (collinear). These multiple scattering paths designated as DST (double scattering triangular), DSC (double scattering collinear) and TSC (triple scattering collinear) by Paktunc and Manceau (2013) are significant in undistorted FeO_6 octahedra based on FEFF8.20 (Ankudinov et al. 1998) simulations performed in butlerite. Uniformity of the Fe-O distances in all the initial precipitates supports this argument and suggests that the FeO_6 octahedra of the precursor oligomeric units are relatively undistorted.

The radial Fe-O distances of the intermediate precipitates are 2.00±0.01 and 2.01±0.01 Å. Following the oxygen shell, there are two Fe shells at 3.05-3.09 Å and 3.49-3.52 Å, and two As shells at 3.18-3.26 Å and 3.37-3.42 Å (Table 5). The shell with shorter Fe-Fe distances is characterized by 1.5-2 Fe and represents edge-sharing FeO_6 octahedra whereas the longer Fe-Fe pairs with 1 Fe are more akin to corner-sharing linkages. The FeO_6 octahedra are linked to 1-1.5 As at 3.18-3.26 Å and 1-2 As at 3.37-3.42 Å. Unlike the initial precipitates, inclusion of the multiple scattering paths did not improve the quality of the fits.

The final precipitates are characterized by slightly longer Fe-O distances at 2.02±0.01 Å. Beyond the O shell, there are 2 Fe shells and 2 As shells composed of 2 atoms each and with radial distances somewhat similar to those of the intermediate precipitates (Table 5). It was possible to include a Ca shell in the fits of the intermediate and final precipitates but the improvements in fit quality were marginal to insignificant.

Thermodynamic properties of arseniosiderite

Chemical composition of the samples. The results of the chemical and TG analyses are summarized in Table 3. The TG traces indicate that arseniosiderite lost essentially all

433 water during the TG run (Fig. 10); therefore, the analytical total is close to 100 %. The
434 calculated formula for arseniosiderite is $Ca_{0.663}Fe_{1.093}(AsO_4)(OH)_{1.605}\cdot 0.827H_2O$, in a
435 good agreement with the compositions of other arseniosiderite precipitates and natural
436 specimens (Tables 1 and 3), and the nominal composition of this mineral, reported as
437 $Ca_2Fe_3(AsO_4)_3O_2\cdot 3H_2O$ (Moore and Araki 1977; Andrade et al. 2012).

438 **Thermodynamic data.** To avoid reporting very large numbers for the complicated
439 and bulky structural formula, all thermodynamic data in this paper are reported as per
440 mole of $Ca_{0.663}Fe_{1.093}(AsO_4)(OH)_{1.605}\cdot 0.827H_2O$ for arseniosiderite (molecular mass
441 268.7229 $g\cdot mol^{-1}$) after normalizing to one mole of AsO_4.

442 **Enthalpies of formation.** Enthalpies of formation were calculated from the
443 calorimetric data via thermochemical cycles (Table 6). The reference compounds were
444 $Ca(OH)_2$, γ-FeOOH, KH_2AsO_4, $HCl\cdot 9.96H_2O$, H_2O, and KCl (all synthetic). We have
445 tested these reference compounds extensively in the past and obtained consistent and
446 accurate data (cf. Majzlan et al. 2003, Majzlan 2011, Majzlan et al. 2012). The only phase
447 that was not tested previously in our laboratory was $Ca(OH)_2$. We have therefore
448 constructed additional thermochemical cycles and checked the accuracy of the dissolution
449 enthalpy with respect to the known data for CaO and $CaSO_4$. Reports of these
450 measurements will be presented in detail elsewhere.

451 Calculated enthalpy of formation from elements at standard conditions are
452 summarized in Table 6.

453 **Heat capacities and entropies.** Heat capacities (C_p) for arseniosiderite were
454 measured from 2 to 302 K. There are a number of features which distinguish the
455 measured data from those of other well-behaved and crystalline phases (Fig. 11). A C_p
456 anomaly which could be assigned to magnetic transition is missing. For a number of Fe
457 arsenates and sulfates, we found such transitions between 5-20 K. It is possible that a
458 magnetic transition occurs in the studied samples below 2 K. A more likely explanation,
459 however, is that the structural disorder prevents magnetic order from being established.

460 The C_p data display an anomalous change in the slope, indicating other than lattice
461 contribution to C_p, at ~140 K. This is probably related to processes in fine-grained or
462 nanocrystalline samples such as changes in the configuration of H_2O molecules on the
463 surfaces of the nanoparticles or onset of molecular motion in the disordered structures.

The nature of the data, especially the broad anomaly, precluded the standard procedures to fit the data. This is especially true in the low-temperature region where C_p can be commonly and with little effort fitted to a Debye or an extended Debye polynomial (e.g. $C_p = B_3T^3 + B_5T^5 + B_7T^7$). The C_p data here cannot be fit with such polynomials because they contain other contributions besides the lattice heat capacity. These contributions could have origin in the magnetic properties or the disorder in the structure and on the surfaces of the nanoparticles.

Because of the anomalous nature of the data, we fit the C_p values by orthogonal polynomials in the entire temperature range and integrated C_p/T to obtain thermodynamic functions. The results at regular temperature intervals are listed in Table 7 and S2.

The disordered state of the samples implies that their configurational entropy is not zero at $T = 0$ K, but it is not quantified with the present data. Hence, the reported entropy (Table 7) is the minimum estimate for arseniosiderite. The configurational entropy could be estimated or quantified from additional thermodynamic data, such as solubility measurements.

The uncertainties for the entropies at $T = 298.15$ K were derived by bootstrap statistics, where the individual data points in the data set are offset within the quoted errors from the measurement and the resulting data set is numerically integrated. We determined the uncertainty on entropy by repeating the procedure more than 1000 times and report the resulting mean C_p/T value with 2 times standard deviation.

Gibbs free energy and stability of arseniosiderite and yukonite. The auxiliary data used for the calculations of thermodynamic data of arseniosiderite and their summaries are listed in Table 8 and 9, respectively. The determination of the thermodynamic data for yukonite was hampered by the silica impurity which is difficult to correct for. Despite that, we derived a rough estimate for the equilibrium constant of the reaction

$$Ca_{1.440}Fe_{2.069}(AsO_4)(OH)_{6.087}\cdot 8.600H_2O\ (yukonite,\ s) + 6.087H^+(aq) = 1.440Ca^{2+}(aq) + 2.069Fe^{3+}(aq) + AsO_4^{3-}(aq) + 14.687H_2O\ (aq)$$

with log K = 6.88 at 25 °C. Those using this value should be forewarned that its uncertainty is large, at least ±3. The magnitude of the uncertainty is not just related to the silica impurity in the sample. The uncertainty in the heat capacity data is a little higher than usual because of the lower signal-to-noise when samples are measured in containers,

as required here due to the vacuum conditions and waters of hydration. Furthermore there is uncertainty due to the unknown configurational entropy which may be large in this case. The equilibria for the two studied minerals are a complex function of temperature and the concentration of ions (H^+, Fe(III), Ca, As(V)) in the aqueous solutions. This work is certainly only a beginning of a thorough description of such equilibria.

DISCUSSION

Precipitation and phase transformations

In general, yukonite and arseniosiderite are the final products precipitating from solutions with initial molar fractions of Ca/(Ca+Fe+As) in the 0.08-0.53 and Fe/(Ca+Fe+As) in the 0.25-0.50 ranges within pH 5-9. These are highly variable concentrations which suggest the importance of these Ca-Fe arsenates in controlling the solution composition at a relatively wide pH range covering slightly acidic to circumneutral and alkaline conditions. Calcium concentrations corresponding to Ca/(Ca+Fe+As) molar fractions as low as 0.08 appear to be adequate for the formation of yukonite. From solutions with 2M Ca, 3M Fe and 3M As, pH conditions between 4.5 and 8 seem to promote the formation of arseniosiderite as the final product whereas yukonite seems to dominate when pH is greater than 8. Yukonite/arseniosiderite begins to form after 13 hours of synthesis at pH 6-8 (Fig. 1) whereas their formation is delayed at higher pH (i.e. ~37 h at pH 9). Continued synthesis beyond 144 hours at pH 9 causes the formation of a Ca arsenate which persists with yukonite for at least one month. Considering that there is no excess Ca in the system, formation of Ca arsenate appears to occur at the expense of yukonite, suggesting that it is dissolving incongruently to yield ferrihydrite.

The precipitate forming from solutions with equal molar proportions of Ca, Fe and As (i.e. 1M each) after about 11-12 days of synthesis is scorodite at pH 4, arseniosiderite at pH 6, a mixture of the two at pH 5, and yukonite and a Ca arsenate at pH 8. In addition, scorodite co-exists with arseniosiderite in the final precipitate from the solution with Ca/(Ca+Fe+As) molar fractions of 0.25 and 0.33 with the Fe/As ratio being at unity at pH~5. Scorodite appears to develop at the expense of arseniosiderite at pH 3 (Table 2). At lower proportions of Fe (i.e. Fe/(Ca+Fe+As)<0.25), johnbaumite and/or an unknown

Ca arsenate is the final precipitate whereas at higher proportions of Fe (i.e. Fe/(Ca+Fe+As)>0.6) ferrihydrite dominates. It appears that ferrihydrite prevents the formation of Ca-Fe arsenates. Instead, a Ca arsenate forms.

Structure of Ca-Fe arsenates

The initial precipitates precursor to yukonite and arseniosiderite are characterized by edge-sharing FeO_6 octahedra that are undistorted. The radial distances for the edge-sharing Fe pairs are 3.03±0.02, 3.04±0.02 and 3.05±0.05 Å which are in agreement with those of Fe colloids and ferrihydrite as summarized by Manceau and Gates (1997). The Fe-As distances (3.33±0.01, 3.34±0.02, 3.35±0.02 Å) are comparable within uncertainty to the As-Fe distances (3.32±0.03, 3.30±0.03, 3.29±0.04 Å) obtained from the As K-edge spectra of the initial precipitates. These fitted parameters suggest that the initial precipitates are made of oligomeric units of edge-sharing FeO_6 octahedra with bridging AsO_4 tetrahedra probably on the opposite polar oxygen atoms (Fig. 12a).

The intermediary and final precipitates possess two Fe-As or As-Fe and two Fe-Fe pairs. Whereas the shorter Fe-Fe distances (3.05-3.13 Å) are indicative of the edge-sharing FeO_6 octahedra, the longer Fe-Fe distances (3.49-3.53 Å) suggest the development of Fe-Fe corner linkages in the intermediary and final precipitates. With As-Fe distances of 3.19-3.21 Å and 3.34-3.35 Å, the presence of two Fe-As pairs in the intermediary and final precipitates is also evident from the As-EXAFS spectra. These local structural data derived from As K-edge and Fe K-edge spectra of the intermediary and final precipitates are compatible with the arseniosiderite structure. In the mitridatite/arseniosiderite structure (Moore and Araki 1976), there are 9 P/As positions, of which 67% are coordinated to 3 Fe atoms and 33% are coordinated to 6 Fe atoms. On average, each P atom is coordinated to 2 Fe at 3.17-3.23 Å, 2 Fe at 3.28-3.41 Å and 2 Ca at 3.58-3.95 Å. Local structural environment of a Fe atom consists of 2 Fe at 3.02-3.13 Å, 2 P at 3.11-3.23 Å, 2 P at 3.28-3.41 Å, 2 Fe at 3.41-3.50 Å and 1.2 Ca at 3.44-3.49 Å. In the structure, edge-sharing FeO_6 octahedra form trigonal rings that are held together and linked by PO_4/AsO_4 tetrahedra. The trigonal rings link at their extreme trigonal corners to the edge midpoints of adjacent rings (Moore and Araki 1976). The rings are composed of 9 edge-sharing FeO_6 octahedra with 9 Fe-Fe distances (3.02-3.13 Å) and 3

pairs of FeO_6 octahedra sharing corners with Fe-Fe distances of 3.41-3.50 Å. The interatomic distances would be longer in arseniosiderite due to longer As-O distances in comparison to P-O distances in mitridatite. Accordingly, the development of Fe-Fe corner linkages evidenced from fitting of the Fe-EXAFS spectra are likely to correspond to the formation of the trigonal rings of the arseniosiderite structure. In this case, it appears that after 24 hours, the initial precipitates characterized by small oligomeric units of edge-sharing FeO_6 octahedra with bridging arsenate evolve to embryonic trigonal rings of FeO_6 nonamers through the establishment of corner linkages between the FeO_6 chains (Fig. 12b). These FeO_6 nonamers are stabilized by an arsenate in the central girdle and bridging arsenate tetrahedra positioned above and below the rings. The Fe-O radial distances of the initial precipitates are tighter at 1.99±0.00 Å (Table 5) suggesting that FeO_6 octahedra are not as much distorted as their counterparts in the later precipitates and that triangular FeO_6 rings have not yet formed in the initial precipitates. The absence of the Fe-Fe corner linkages and As-Fe distances of 3.29-3.32 Å in the initial precipitates supports this hypothesis. The changes in the local structure with synthesis time is in part due to the distortion of the FeO_6 octahedra resulting from the formation of the trigonal rings of octahedra held together by an arsenate tetrahedron in the central girdle coordinated to six FeO_6 octahedra and three arsenate tetrahedra bridging three FeO_6 octahedra forming the corners of the trigonal ring (Fig. 12b).

Appearance of the initial peaks of yukonite/arseniosiderite, corresponding to *hkl* peaks of (162), (033), (031), (166) and (182), is delayed at higher pH (i.e ~37 h at pH 9) as opposed to ~13 h at pH 6-8 (Fig. 1). Faster development of the crystallinity with a decrease in the solution pH is further evidenced from the shift of the low angle peak at ~12 Å to lower *d*-spacings (Fig. 2). The precipitates forming at pH 6, 7 and 8 have a low-angle peak at 9-10 Å, which is between the yukonite peak at 14 Å, and arseniosiderite peak at 8.8 Å. This peak corresponds to the layers of Fe octahedra in the arseniosiderite structure (Fig. 12c) which begins to develop after about 37 h and gradually moves to shorter *d*-spacings with continued synthesis. In other words, interlayers in yukonite are widely spaced or loosely bound and they begin to tighten up with increased crystallinity. In essence, yukonite and arseniosiderite are the same mineral species with variable degree of crystallinity, confirming the earlier contention of Paktunc et al. (2003) and (2004).

Formation of clusters of arseniosiderite after 24 hours with the crystallite sizes of ~5×15 nm is supported by HRTEM observations such as the development of lattice fringes with interlayer spacings of 0.94-1.03 nm (Fig. 5). These correspond to the closure of interlayer *d*-spacings from powder XRD results. Yukonite specimens from the Daulton Mine, Ketza River mine (Table 1) and those reported earlier by Dunn (1982), Ross and Post (1997) and Garavelli et al. (2009) have lower Ca concentrations in comparison to the arseniosiderite specimens listed in Table 1 and the nominal arseniosiderite composition. On average, yukonite has a deficiency of 0.3 to 0.8 Ca per formula unit. This deficiency is probably a reflection of the lower site occupancies in the interlayer components of yukonite. Persistence of yukonite at higher pH without the development of interlayer components is probably arising from the limitations on the activity of Ca connecting the layers formed by octahedral and tetrahedral sheets. This would limit the development of the sheet stacking evidenced from the limited number of octahedral layers (i.e. between 4 and 6 for ~15 nm long particles). Persistence of yukonite at pH > 8 is also supported by the thermodynamic data (Fig. 15) which show that the difference in the solubilities of yukonite and arseniosiderite is much lower in this pH range than under the acidic conditions.

Natural analog of phase transformations

In the Ketza River gold mine, gold mineralization occurs as sulfide and oxide bodies with the oxide ore believed to have resulted from the oxidation of sulfide minerals during a paleoweathering event (Stroshein 1996; Fonseca 1998). The transition between the two ore bodies provides a unique geological setting for studying mineralogical transformations during the formation of the oxide ore. Accordingly, the transition zone would serve as a natural analog for mineralogical transformations that will take place over time in arsenical mine wastes and guide efforts in predicting future arsenic releases from the wastes.

Previous studies at the Ketza River mine site have identified a complex assemblage of As-bearing minerals in the ore, processing products and mine tailings including arsenopyrite, scorodite, amorphous ferric arsenate, As-rich goethite, amorphous Ca-Fe arsenate, arseniosiderite, yukonite, As-bearing jarosite, pharmacosiderite, and rooseveltite

(Paktunc et al., 2003, 2004). In the oxide ore, arsenopyrite is progressively replaced by scorodite during a pervasive event where As is redistributed in large continuous aggregates of scorodite that forms pseudomorphs after arsenopyrite (Fig. 13a) or fills veins and fractures (Fig. 13b). Ca-Fe arsenates occur as massive and leaf-like or flaky aggregations in spheroidal arrangements and as replacement products of arsenopyrite and scorodite (Paktunc et al. 2003, 2004). Textural features showing replacement of scorodite by yukonite and arseniosiderite are common in the Ketza River ore and rocks. Although scorodite appears to be stable in most oxidized rocks investigated, there are instances, where there is progressive replacement of scorodite initiated at the pore interface (Fig. 14a). Scorodite transformation was characterized structurally by micro-XRD analyses at four representative locations across a transition labeled L1 to L3 in Figure 14. Moving outwards from pristine scorodite towards the replacement product at the pore interface, there is a progressive change from a randomly oriented well-crystallized scorodite (L1) with sharp uniform diffraction rings to a poorly crystalline phase with diffuse diffraction bands (L2) becoming slightly sharper within the pore (L4). The diffraction patterns obtained by integrating the rings in the images are compared with simulated patterns of scorodite, yukonite, arsenisiderite and goethite in Figure 14b. The patterns indicate the replacement of well-crystallized fine-grained scorodite ultimately to yukonite at the interface (L2, L3), and the growth of fibrous arseniosiderite lining the pore (L3, L4). Electron probe microanalyses of this material growing freely within the pores confirm that it is arseniosiderite with the following formula: $Ca_2Fe_3(AsO_4)_{2.7}(SiO_4)_{0.1}(OH)_x \cdot yH_2O$ (Table 10). Within the area dominated by yukonite, a distinct band appearing brighter in the backscattered electron images is observed (L3 in Fig. 14a). Characterization by micro-XRD of the region straddling this material indicates that it consists of goethite coexisting with surrounding arseniosiderite and yukonite.

Quantitative Fe Kα, Ca Kα, and As Lα X-ray maps collected by an electron probe microanalyzer from the scorodite-yukonite transition zone are shown in Figure 14c. The increase in Ca at the scorodite replacement front is very sharp and initial interstitial replacement within the scorodite aggregate can be observed. At the replacement front, there is a sharp increase in the Fe/As ratio, which then progressively decreases back to values closer to unity. The band identified as goethite by micro-XRD has ~7 wt % As and

650 ~2.5 wt % Ca. In contrast, the Ca/As ratio is much less variable from the replacement
651 front towards the pore with a value close to 2/3. The representative analyses show that a
652 Ca/As ratio of 2/3 is instantly reached at the scorodite replacement front and remains
653 essentially constant up to the pore interface. Composition of the yukonite phase
654 determined by EPMA near the pore interface is $Ca_{1.7}Fe_3(AsO_4)_{2.8}(SiO4)_{0.1}(OH)_x \cdot yH_2O$
655 (Table 10). It appears that scorodite transformation to arseniosiderite is gradual through
656 the formation of yukonite.
657
658 **Implications for arsenic mobility**
659 The findings of this study suggest that arseniosiderite and yukonite are likely to form
660 from solutions rich in Ca, Fe(III) and As which may arise from lime neutralization of
661 metallurgical effluents and acid mine drainage resulting from the oxidation of As-bearing
662 sulfides such as arsenopyrite and As-pyrite. In addition, interaction of Ca-rich solutions
663 such as gypsum-saturated neutralization sludge with mine tailings containing scorodite
664 and amorphous ferric arsenate would promote the formation of Ca-Fe arsenates in mine
665 environments. Arseniosiderite and yukonite also occur in naturally polluted soils (e.g.,
666 Drahota et al. 2009). They are excluded from acidic to nearly neutral environments in
667 which they dissolve readily and transform to scorodite or iron oxides with
668 adsorbed/incorporated arsenic, respectively (Figs. 15, 16). There are sites, however,
669 where arsenic mobilization is controlled by the Ca-Fe arsenates. It is therefore instructive
670 to examine the thermodynamic solubility of arseniosiderite and compare the results to the
671 solubility of other common arsenic-bearing phases.
672 The equilibrium molalities of arsenic and iron in aqueous solutions in contact with a
673 number of common minerals are shown in Fig. 15. From the phases considered, the best
674 performance in terms of immobilization of arsenic can be attributed to scorodite at acidic
675 conditions and As-HFO at mildly acidic, circumneutral, and alkaline conditions.
676 Arseniosiderite performs comparably to mimetite and as such it would be a suitable phase
677 to keep the equilibrium arsenic concentrations below 0.5 mg/L within pH 4.5-10.5 for the
678 Canadian metal mining effluent regulation and below 0.2 mg/L within pH 5-9.5 for the
679 Québec provincial mine effluent guideline. This is a rather wide pH range, partly
680 overlapping and complementing the control imposed by scorodite solubility within pH

2.5-7. Incongruent dissolution of scorodite and its precursor amorphous ferric arsenate at pH>~2.5 with concomitant precipitation of ferrihydrite would continuously promote the dissolution of scorodite and ferric arsenate by driving the solution composition to undersaturation with respect to scorodite (Majzlan 2011) and ferric arsenate (Paktunc et al. 2008). The order of stability of scorodite and arseniosiderite in terms of pH and Ca concentrations (Fig. 16) is in agreement with our synthesis experimental results. Higher Ca activity is required for the transformation of scorodite to arseniosiderite. Otherwise, formation of goethite at the expense of scorodite would cause As releases. Our findings confirm the dissolution behaviour of scorodite under gypsum-saturated conditions with lower equilibrium As concentrations (Bluteau et al. 2009). Johnbaumite and yukonite are highly soluble; we recall again that the data for yukonite are hampered with a large uncertainty.

A similar picture is portrayed for the equilibrium molalities of iron in solutions. Here, the solubility curve of goethite is also shown to document the solubility difference between a well-crystalline iron oxide (goethite) and a poorly crystalline iron oxide (HFO).

Behaviour of arseniosiderite in solutions buffered by scorodite and a soluble Ca mineral such as calcite, anorthite, gypsum or Ca-montmorillonite can be assessed in Figure 17 where saturation index of arseniosiderite is shown as a function of pH. The aqueous solution in contact with scorodite becomes saturated with respect to arseniosiderite in the pH range of 4-6, depending on the Ca-bearing mineral. The cases with anorthite and Ca-montmorillonite would be relevant for weathering soil profiles developing over crystalline rocks hosting quartz-pyrite-arsenopyrite-gold ores.

With these considerations, it appears that the formation of arseniosiderite would be desirable for controlling As concentrations in mine wastes and contaminated soil. Neutralization sludge from water treatment plants or solutions buffered by a soluble Ca mineral would provide the means for arseniosiderite precipitation. Likewise, disposal of tailings containing arseniosiderite and those with scorodite in lime-treated or gypsum-saturated effluents may prove to be effective for limiting As mobilization from the mine wastes provided that circumneutral pH conditions are maintained. Similarly, disposal conditions favouring progressive replacement of scorodite and ferric arsenate by

arseniosiderite can be considered as an alternate design option for waste management facilities.

CONCLUSIONS

Yukonite and arseniosiderite form from solutions with initial molar proportions of Ca/(Ca+Fe) in the 0.25-0.75 and Fe/(Fe+As) in the 0.27-0.67 ranges within pH 5 to 9. Calcium concentrations corresponding to molar Ca/(Ca+Fe+As) ratios as low as 0.1 appear to be adequate for the formation of yukonite and arseniosiderite. Arseniosiderite coexists with scorodite at pH 5. Higher initial Fe concentrations promote the formation of ferrihydrite which prevents the formation of Ca-Fe arsenates. Formation of Ca arsenates including johnbaumite and $Ca_3(AsO_4)_2 \cdot 2.3H_2O$ is restricted to starting pH of 8.5-10 and lower initial solution concentrations of Fe.

The initial Ca-Fe arsenate precipitates are characterized by two broad humps at about 2.90 and 1.58 Å *d*-spacings, resembling the amorphous ferric arsenate (3.0 and 1.56 Å). They occur as large lumpy agglomerations of smaller particles with no internal structure discernable in high-resolution TEM images suggesting that they are largely amorphous. These amorphous precipitates transform to yukonite after about 13 hours of synthesis at pH≤8 and 24 h at pH 9, and to arseniosiderite after about 37 h at pH 6, 7 and 8. Transformation of yukonite to arseniosiderite is greatly delayed at pH 9. Transformation to yukonite coincides with the development of prominent lattice fringes representing the FeO_6 octahedral layers sandwiched between arsenate tetrahedra of the arseniosiderite structure. It appears that arseniosiderite forms at a wide pH range but its formation is kinetically controlled.

The initial amorphous precipitate precursors to yukonite and arseniosiderite are made of small polymeric units of undistorted edge-sharing FeO_6 octahedra with bridging AsO_4 tetrahedra on the opposite polar oxygen atoms. The intermediary and final precipitates have slightly longer Fe-O distances, and possess two Fe-As and two Fe-Fe pairs. Whereas the shorter Fe-Fe distances are indicative of the edge-sharing FeO_6 octahedra, the longer Fe-Fe distances represent Fe-Fe corner linkages suggesting the development of crystallinity. These local structural data are compatible with the structure of arseniosiderite. It appears that the initial small oligomeric units of edge-sharing FeO_6

743 octahedra with bridging arsenate evolve to embryonic trigonal rings of FeO_6 nonamers
744 through the establishment of corner linkages between the FeO_6 chains. Yukonite
745 possesses a structure that is similar to its successor, arseniosiderite. Yukonite represents a
746 nanocrystalline variety with a deficiency of 0.3 to 0.8 Ca per formula unit which is
747 probably reflecting lower site occupancies in the interlayer components of yukonite.
748 Development of interlayer components leading to the formation of arseniosiderite is
749 delayed with increased pH. Lower pH conditions appear to accelerate the development of
750 crystallinity from yukonite to arseniosiderite.

751 Arseniosiderite and yukonite are the likely compounds to form from lime
752 neutralization of acid mine drainage and effluents rich in As. Formation of yukonite and
753 arseniosiderite from highly variable solution concentrations at a wide pH range from
754 slightly acidic to alkaline conditions suggests the importance of these minerals in
755 controlling As concentrations in near-surface environments saturated with respect to
756 soluble Ca minerals. Our experimental results confirm observations in natural settings
757 and mine tailings where scorodite is progressively replaced by yukonite and its
758 transformation to arseniosiderite.

759 The solubility product of arseniosiderite is –21.60±0.76 (referring to the reaction in
760 Table 9). Its relatively low solubility would prevent the equilibrium arsenic
761 concentrations from exceeding the Canadian mine effluent regulatory guidelines within a
762 relatively wide pH range from about 4.5 to 10.5. However, our thermodynamic data
763 indicate that the arseniosiderite stability field does not extend into alkaline conditions
764 beyond the circumneutral pH. With the controls imposed by scorodite within pH 2.5-7,
765 conditions promoting the formation of arseniosiderite would be desirable for effective As
766 controls. Incongruent dissolution of scorodite with undesirable consequences in terms of
767 As releases can be avoided by the formation of arseniosiderite because replacement of
768 scorodite by arseniosiderite does not involve the formation of an Fe(III) oxyhydroxide.
769 In other words, dissolution of scorodite in Ca-rich solutions and simultaneous formation
770 of arseniosiderite would prevent As releases unlike the situation where scorodite
771 dissolves incongruently above pH~2.5 in undersaturated solutions with respect to
772 common soluble Ca compounds.

773 Conditions promoting the formation of arseniosiderite would be desirable in mine
774 wastes and contaminated soil to limit As releases. Accordingly, the study results can be
775 used to better assess the integrity of mine tailings and sludge in terms of arsenic releases
776 and the potential for groundwater contamination. The results will also lead to the
777 development of new and improved technologies for As control and stabilization in mine
778 wastes. Lime-treated or gypsum-saturated ferric arsenate solutions such as neutralization
779 sludge can be engineered to lead to the formation of arseniosiderite to effectively stabilize
780 arsenic in tailings impoundments.

781 **ACKNOWLEDGEMENTS**

782 Parts of the synthesis work reported in this manuscript were carried out during 2007-
783 09 as part of an MSc thesis research by A.H. under the supervision of the lead author. We
784 acknowledge British Museum and Peter Swash (Imperial College, now with Alcoa) for
785 donating the yukonite and arseniosiderite specimens, John Chaulk and Derek Smith
786 (Canmet) for helping with the experimental and characterization work, Andreas Korinek
787 (Canadian Centre for Electron Microscopy at McMaster University) for providing help
788 with the TEM characterization, Robert Gordon (PNC-CAT, Advanced Photon Source)
789 for helping with the EXAFS experiments. We thank F. Bellmann for the permission to
790 use his value of the dissolution enthalpy of $Ca(OH)_2$. The EXAFS measurements at APS
791 were carried out under a General User Proposal to the senior author and a Partner User
792 Proposal supported by the Natural Sciences and Engineering Research Council (NSERC)
793 of Canada through a major facilities access grant. Research at the PNC-CAT beamline of
794 APS, Argonne National Laboratory is supported by the US Department of Energy under
795 Contracts W-31-109-Eng-38 (APS) and DE-FG03- 97ER45628 (PNC-CAT). The study
796 was funded by an NSERC Discovery Grant and a Natural Resources Canada grant to the
797 lead author. We also acknowledge the Canada Foundation for Innovation, the Atlantic
798 Innovation Fund, and other partners which fund the Facilities for Materials
799 Characterization, managed by the Institute for Research in Materials at Dalhousie
800 University, for time on the PPMS. The work of J.M. was financially supported by the
801 project INFLUINS (Grant Nr. 03IS2091A) by the German Ministry of Education and
802 Research (BMBF) within the program Spitzenforschung und Innovation in den Neuen

Ländern. We thank the journal referees, Kirk Nordstrom and an anonymous reviewer for their careful reviews with detailed and constructive comments, and Lynda Williams for editorial handling of the manuscript.

REFERENCES CITED

Andrade, M.B., Morrison, S.M., Domizio, A.J.D., Feinglos, M.N., and Downs, R.T. (2012) Robertsite, $Ca_2Mn^{III}_3O_2(PO_4)_3 \cdot 3H_2O$. Acta Crystallographica, E68, i74-i75.

Ankudinov, A.L., Ravel, B., Rehr, J.J., and Conradson, S.D. (1998) Real-space multiple-scattering calculation and interpretation of x-ray-absorption near-edge structure. Physical Review B, 58, 7565−7576.

Bluteau, M-C., Becze, L., and Demopoulos, G.P. (2009) The dissolution of scorodite in gypsum-saturated waters: Evidence of Ca–Fe–AsO_4 mineral formation and its impact on arsenic retention. Hydrometallurgy, 97, 221-227.

Burlak, T.L. (2012) The mineralogical fate of arsenic during weathering of sulfides in gold-quartz veins: A microbeam analytical study. M.Sc. Thesis, California State University, Sacremento, 142p.

Cancès, B., Juillot, F., Morin, G., Laperche, V., Polya, D., Vaughan, D.J., Hazemann, J.-L., Proux, O., Brown, G.E., and Calas, G. (2008) Changes in arsenic speciation through a contaminated soil profile: A XAS based study. Science of the Total Environment, 397, 178-189.

Drahota, P., Rohovec, J., Filippi, M., Mihaljevic, M., Rychlovsky, P., Cerveny, V., and Pertold, Z. (2009) Mineralogical and geochemical controls of arsenic speciation and mobility under different redox conditions in soil, sediment and water at the Mokrsko-West gold deposit, Czech Republic. Science of the Total Environment, 407, 3372-3384.

Dunn, P.J. (1982) New data for pitticite and a second occurrence of yukonite at Sterling Hill, New Jersey. Mineralogical Magazine 46, 261-264.

Dunn, P.J., Peacor, D.R., and Newberry, N. (1980) Johnbaumite, a new member of the apatite group from Franklin, new Jersey. American Mineralogist 65, 1143-1145.

Filippi, M., Dous□ová, B., and Machovic□, V. (2007) Mineralogical speciation of arsenic in soils above the Mokrsko–west gold deposit, Czech Republic. Geoderma, 139, 154–70.

Fonseca, A.L. (1998) Origin of Carbonate-Hosted Gold Rich Replacement Deposits and Related Mineralization Styles in the Ketza River Deposit, Yukon Territory. M.Sc. Thesis, University of British Columbia, 109p.

Foster, A.L., Ashley, R.P., and Rytuba, J.J. (2011) Arsenic species in weathering mine tailings and biogenic solids at the Lava Cap Mine Superfund Site, Nevada City, CA. Geochemical Transactions, 12, 1-21.

Gomez, M.A., Becze, L., Blyth, R.I.R., Cutler, J.N., and Demopoulos, G.P. (2010) Molecular and structural investigation of yukonite (synthetic & natural) and its relation to arseniosiderite. Geochimica et Cosmochimica Acta, 74, 5835-5851.

Garavelli, A., Pinto, D., Vurro, F., Mellini, M., Viti, C., Balic-Zunic, T., and Della Ventura, G. (2009) Yukonite from the Grotta Della Monaca cave, Sant'agata di Esaro, Italy: Characterization and comparison with cotype material from the Daulton Mine, Yukon, Canada. Canadian Mineralogist, 47, 39-51.

Kennedy, C.A., Stancescu, M., Marriott, R.A., and White, M.A. (2007) Recommendations for accurate heat capacity measurements using a Quantum Design physical property measurement system. Cryogenics, 47, 107-112.

Kim, C.S., Stack, D.H., and Rytuba, J.J. (2012) Fluvial transport and surface enrichment of arsenic in semi-arid mining regions: examples from the Mojave Desert, California. Journal of Environmental Monitoring, 14, 1798-1813.

Krause, E. and Ettel, V.A. (1989) Solubilities and stabilities of ferric arsenate compounds. Hydrometallurgy, 22, 311–337.

Majzlan, J. (2011) Thermodynamic Stabilization of Hydrous Ferric Oxide by Adsorption of Phosphate and Arsenate. Environmental Science and Technology, 45, 4726-2732.

Majzlan, J., Grevel, K.-D., and Navrotsky, A. (2003) Thermodynamics of iron oxides: Part II. Enthalpies of formation and relative stability of goethite (α-FeOOH), lepidocrocite (γ-FeOOH), and maghemite (γ-Fe_2O_3). American Mineralogist, 88, 855-859.

Majzlan, J., Mazeina, L., and Navrotsky, A. (2007) Enthalpy of water adsorption and surface enthalpy of lepidocrocite (γ-FeOOH). Geochimica et Cosmochimica Acta 71, 615-623.

Majzlan, J., Drahota, P., Filippi, M., Grevel, K.-D., Kahl, W.-A., Plášil, J., Woodfield, B.F., and Boerio-Goates, J. (2012) Thermodynamic properties of scorodite and parascorodite ($FeAsO_4 \cdot 2H_2O$), kaňkite ($FeAsO_4 \cdot 3.5H_2O$), and $FeAsO_4$. Hydrometallurgy, 117-118, 47-56

Manceau, A. and Gates, W.P. (1997) Surface structural model for ferrihydrite. Clays and Clay Minerals, 45, 448-460.

Manceau, A., Lanson, M., and Geoffroy, N. (2007) Natural speciation of Ni, Zn, Ba, and As in ferromanganese coatings on quartz using X-ray fluorescence, absorption, and diffraction. Geochimica et Cosmochimica Acta, 71, 95–128.

Marriott, R.A., Stancescu, M., Kennedy, C.A., and White, M.A. (2006) Technique for determination of accurate heat capacities of volatile, powdered or air-sensitive samples using relaxation calorimetry. Review of Scientific Instruments, 77, 096108-1 – 096108-3.

Moore, P.B. and Araki, T. (1976) Mitridatite, $Ca_6(H_2O)_6[Fe^{III}_9O_6(PO_4)_9] \cdot 3H_2O$. A noteworthy octahedral sheet structure. Inorganic Chemistry, 16, 1096-1106.

Nishikawa, O., Okrugin, V., Belkova, N., Saji, I., Shiraki K., and Tazaki, K. (2006) Crystal symmetry and chemical composition of yukonite: TEM study of specimens col- lected from Nalychevskie hot springs, Kamchatka, Russia and from Venus mine, Yukon Territory, Canada. Mineralogical Magazine, 70, 73-81.

Nordstrom, D.K. and Munoz, J.L. (1994) Geochemical Thermodynamics, 2nd edition. Blackwell Scientific Publications.

Nordstrom, D.K., Majzlan, J., and Königsberger, E. (2014) Thermodynamic Properties for Arsenic Minerals and Aqueous Species. Reviews in Mineralogy and Geochemistry, doi.org/10.2138/rmg.2014.79.4

Paktunc, D. and Manceau, A. (2013) Comment on "New Clues to the Local Atomic Structure of Short-Range Ordered Ferric Arsenate from Extended X‑ray Absorption Fine Structure Spectroscopy". Environmental Science and Technology 47, 13199−13200.

Paktunc, A. D., Foster, A., and Laflamme, J. (2003) Speciation and characterization of arsenic in Ketza River Mine tailings using X-ray absorption spectroscopy. Environmental Science and Technology, 37, 2067– 2074.

Paktunc, D., Dutrizac, J., and Gertsman, V. (2008) Synthesis and phase transformations involving scorodite, ferric arsenate and arsenical ferrihydrite: Implications for arsenic mobility. Geochimica et Cosmochimica Acta, 72, 2649-2672.

Paktunc, D., Foster, A., Heald, S., and Laflamme, G. (2004) Speciation and characterization of arsenic in gold ores and cyanidation tailings using X-ray absorption spectroscopy. Geochimica et Cosmochimica Acta, 68, 969–983.

Paktunc, D., Majzlan, J., Dutrizac, J., Palatinus, L., Klementová, M., and Poirier, G. (2013) Characterization of ferric arsenate-sulphate compounds with implications on arsenic control in refractory gold processing residues. American Mineralogist, 98, 554-565.

Parker, V.B. (1965) Thermal properties of uni-univalent electrolytes. National Standard Reference Data Series, National Bureau of Standards, 2, 66 pp.

Parkhurst, D.L. and Appelo, C.A.J. (1999) User's guide to PHREEQC (Version 2)--a computer program for speciation, batch-reaction, one-dimensional transport, and inverse geochemical calculations: U.S. Geological Survey Water-Resources Investigation Report, 99-4259, 312 pp.

Pieczka, A., Golebiowska, B., and Franus, W. (1998) Yukonite, a rare Ca-Fe arsenate, from Redziny (Sudetes, Poland). European Journal of Mineralogy, 10, 1367-1370.

Ravel, B. and Newville, M. (2005) ATHENA, ARTEMIS, HEPHAESTUS: data analysis for X-ray absorption spectros- copy using IFEFFIT. Journal of Synchrotron Radiation, 12, 537–541.

Rehr, J.J, Mustre de Leon, J., Zabinsky, S.I., and Albers, R.C. (1991) Theoretical X-ray Absorption Fine Structure Standards. Journal of American Chemical Society, 113, 5135.

Robie, R.A. and Hemingway, B.S. (1995) Thermodynamic properties of minerals and related substances at 298.15 K and 1 bar (10^5 Pascal) pressure and at higher temperatures. U. S. Geological Survey Bulletin, 2131, 461 p.

924 Robins, R.G. and Tozawa, K. (1982) Arsenic removal from gold processing waste waters:
925 the potential influence of lime. CIM Bulletin, 75, 171-174.
926 Ross, D.R. and Post, J.E. (1997) New data on yukonite. Powder Diffraction, 12, 113-116.
927 Stroshein, R. (1996) Geology and gold deposits at Ketza River, Yukon Territory, a
928 progress report. In: Yukon Exploration and Geology 1995, Exploration and
929 Geological Services Division, Yukon, Indian and Northern Affairs Canada, 43-48.
930 Swash, P.M. and Monhemius, A.J. (1994) Hydrothermal precipitation from aqueous
931 solutions containing iron (III), arsenate and sulphate. In: Proceedings International
932 Symposium Hydrometallurgy'94. Chapman & Hall, New York, pp. 177–190.
933 Swash, P.M. and Monhemius, A.J. (1995) Synthesis, characterization and solubility
934 testing of solids in the Ca-Fe-AsO_4 system. In: Proceedings Conference on Mining
935 and the Environment, Sudbury'95. Vol 1, pp. 17–28.
936 Tyrell, J.B. and Graham, R.P.D. (1913) Yukonite, a new hydrous arsenate of iron and
937 calcium, from Tagish Lake, Yukon Territory, Canada: with a note on the associated
938 symplesite. Transactions of the Royal Society of Canada, 7, 1-9.
939 Walker, S.R., Parsons, M.B., Jamieson, H.E., and Lanzirotti, A. (2009) Arsenic
940 mineralogy of near-surface tailings and soils: Influences on arsenic mobility and
941 bioaccessibility in the Nova Scotia gold mining districts. Canadian Mineralogist,
942 47, 533-556.

943 **FIGURE CAPTIONS**

944 **FIGURE 1.** XRD patterns of the precipitates formed during batch synthesis experiments
945 at starting pH 6 (a), pH 7 (b), pH 8 (c) and pH 9 (d). Numbers next to XRD patterns are
946 synthesis times in hours. Patterns are shifted along vertical axes without changing
947 intensity scales. asd: arseniosiderite.

948 **FIGURE 2.** Changes with synthesis time in *d*-spacings of the low-angle peak of
949 arseniosiderite at starting pH values of 6, 7 and 8.

950 **FIGURE 3.** XRD patterns of the final precipitates formed during continuous synthesis
951 experiments at pH 4.5 (C03) and pH 8.5 (C04) (a), and initial, intermediary and final
952 precipitates formed during continuous synthesis at pH 9 (C05) (b). Numbers next to XRD
953 patterns in b are synthesis times in hours. Patterns are shifted along vertical axes without
954 changing intensity scales. asd: arseniosiderite; yuk: yukonite.

955 **FIGURE 4.** High-resolution TEM image of the initial precipitate of amorphous Ca ferric
956 arsenate formed at pH 8 after 1 hour showing no discernable internal structures.

957 **FIGURE 5.** High-resolution TEM images of the intermediary yukonite precipitates
958 formed at pH 6, 7 and 8 showing lath-shaped nanocrystals with prominent lattice fringes
959 corresponding to (100) of arseniosiderite. (a) pH 6, 13 h; (b) pH 7, 13 h; (c) pH 6, 24 h;
960 (d) pH 8, 24h.

961 **FIGURE 6.** k^3-weighted As *K*-edge EXAFS spectra of the precipitates formed during
962 batch synthesis at pH 6 (K09), pH 7 (K10) and pH 8 (K11). Numbers following the dash
963 are synthesis time in hours. Experimental spectra shown in black solid lines and
964 simulations in red circle lines. Uniform vertical scales in all.

965 **FIGURE 7.** Fourier transforms of As *K*-edge EXAFS spectra shown in Fig 6. Uniform
966 vertical scales in all.

967 **FIGURE 8**. k^3-weighted Fe *K*-edge EXAFS spectra of the precipitates formed during
968 batch synthesis at pH 6 (K09), pH 7 (K10) and pH 8 (K11), and continuous synthesis at
969 pH 4.5 (C03). Numbers following the dash are synthesis time in hours. Experimental
970 spectra shown in black solid lines and simulations in red circle lines. Uniform vertical
971 scales in all.

972 **FIGURE 9.** Fourier transforms of Fe *K*-edge EXAFS spectra shown in Fig.8. Uniform
973 vertical scales in all.

974 **FIGURE 10.** Mass loss curves for arseniosiderite (solid curve) and yukonite (dashed
975 curve).
976 **FIGURE 11.** Measured heat capacity data for arseniosiderite using two pellets weighing
977 8.69 mg and 7.11 mg.
978 **FIGURE 12.** Polyhedral representations of (a) initial precipitates characterized by edge-
979 sharing FeO_6 octahedra (brown) and bridging AsO_4 tetrahedra (purple), (b) intermediary
980 precipitates characterized by the formation of trigonal rings of FeO_6 nonamers through
981 the establishment of Fe-Fe corner linkages between FeO_6 trimers or tetramers, (c)
982 intermediary and final precipitates with the development of layers along (100) with blue
983 balls representing Ca, and (d) HRTEM image showing well-developed lattice fringes
984 representing (100) along with the polyhedral representation of the layers as in "c" scaled
985 to the layers in the HRTEM image.
986 **FIGURE 13.** Backscattered electron images showing typical habit displayed by
987 scorodite. Pseudomorphs after arsenopyrite (a), and pervasive veins and fracture filling in
988 quartz (b).
989 **FIGURE 14.** (a) Backscattered electron image showing progressive replacement of
990 scorodite (bright major phase) at a pore interface; (b) Debye ring images obtained by
991 micro-XRD at locations L1, L2 and L4 (30 μm collimator) and background-subtracted
992 diffraction patterns obtained by integrating the Debye rings (Cr Kα radiation, wavelength
993 2.2896 Å); (c) Quantitative Fe Kα, Ca Kα and As Lα X-ray maps acquired from the area
994 outlined by white square in a.
995 **FIGURE 15.** Solubility curves for selected arsenate and oxide minerals. The calculated
996 molalities of As(V) (left) and Fe(III) (right) are plotted on the logarithmic scale as a
997 function of the pH of the aqueous phase.
998 **FIGURE 16.** Stability fields of the minerals scorodite, goethite, and arseniosiderite in the
999 pH-$a(Ca^{2+})$ space. log a(Fe(III)) = –7, log a(As(V)) = –4.
1000 **FIGURE 17.** Saturation indices of arseniosiderite and yukonite, calculated from
1001 thermodynamic simulations performed with the PHREEQC software (Parkhurst and
1002 Appelo 1996). An aqueous solution with a predetermined pH was allowed to equilibrate
1003 with atmospheric O_2 and these two minerals: (1) scorodite+gypsum (black curves), (2)
1004 scorodite+calcite (red), (3) scorodite+anorthite (green) and (4) scorodite+Ca-

1005 montmorillonite (cyan). Afterwards, the saturation indices for the two Ca-Fe arsenates
1006 were calculated. The upper bundle of the curves represents the saturation indices for
1007 arseniosiderite, the lower bundle the indices for yukonite. Note that scorodite is unstable
1008 above pH of ~3 and will dissolve incongruently (see Majzlan et al. 2012 for a detailed
1009 discussion). The diagrams shown here are meant as approximate guides to the conditions
1010 under which an aqueous solution can become supersaturated with respect to
1011 arseniosiderite or yukonite.
1012

Table 1. Compositions of yukonite and arseniosiderite

	Las Animas Sonora arseniosiderite	Daulton Mine Yukon yukonite	Ketza River Mine, Yukon arseniosiderite	Ketza River Mine, Yukon yukonite
n	30	15	41	13
wt%				
Fe_2O_3	31.74±0.74	36.05±4.64	31.44±0.80	33.26±1.78
MnO	0.25±0.05	0.34±0.07	0.04±0.05	0.33±0.30
CaO	14.77±0.33	11.56±1.31	14.46±0.31	11.62±1.04
Al_2O_3	0.02±0.02	0.15±0.04	0.04±0.06	0.06±0.10
As_2O_5	36.95±0.48	37.15±3.90	42.55±1.26	36.82±2.34
SiO_2	3.63±0.15	0.40±0.15	0.22±0.24	0.90±0.61
Na_2O	0.11±0.01	0.13±0.04	*na*	*na*
formula				
Fe	3.0	3.0	3.0	3.0
Mn	0.0	0.0	0.0	0.0
Ca	2.0	1.4	2.0	1.5
Al	0.0	0.0	0.0	0.0
AsO_4	2.4	2.1	2.8	2.3
SiO_4	0.5	0.0	0.0	0.1
Na	0.0	0.0		
OH	3.9	5.1	4.3	4.6
H_2O	3.3	2.2	2.6	4.4

Mineral formula based on 17 O recast to 3 Fe; OH and H_2O calculated to maintain charge balance; *n:* number of grains analysed; *na*: not analysed.

Table 2. Summary of synthesis experiments

Label	Ca:Fe:As (M)	pH	Time (h)	color	phase
Batch synthesis					
A01	1 : 1 : 1	8.2	0	7.5YR 6/6	cfa
		8.1	264	10YR 5/6	ca
A03	2 : 1 : 1	9.4	0	7.5YR 6/6	jbm
		8.7	96	7.5YR 5/6	jbm
A04	1 : 2 : 1	8.5	0	7.5YR 5/6	cfa
		7.6	96	7.5YR 5/6	yuk
A09	1 : 3 : 1	8.4	0	5YR 4/4	cfa
		7.6	96	7.5YR 4/4	cfa
A10	3 : 1 : 1	8.2	0	10YR 7/6	cfa
		7.5	96	10YR 4/4	yuk+ca
A12	1 : 2 : 2	9.0	0	5YR 5/6	cfa
		7.9	96	7.5YR 4/6	yuk
A13	2 : 2 : 1	8.3	0	7.5YR 5/6	cfa
		7.6	96	7.5YR 4/6	yuk
A14	1 : 2 : 3	8.5	0	7.5YR 6/6	cfa
		7.9	96	10YR 4/6	yuk
A15	3 : 1 : 8	8.5	0	10YR 8/3	jbm
		8.0	96	10YR 8/6	jbm
A16	1 : 3 : 8	8.2	0	7.5YR 7/6	cfa
		7.7	96	10YR 3/4	yuk
A18	8 : 3 : 4	8.4	0	7.5YR 7/4	cfa
		7.4	96	10YR 5/4	yuk+ca
A19	8 : 4 : 3	9.1	0	7.5YR 6/6	cfa
		8.3	96	7.5YR 4/6	yuk
A20	7 : 2 : 5	8.9	0	10YR 8/3	cfa
		6.1	96	2.5YR 7/4	ca
A26	7 : 1 : 5	9.5	0	7.5YR 8/4	jbm
		8.0	96	7.5YR 8/6	jbm
A28	14 : 1 : 10	9.2	0	7.5YR 8/4	jbm
		7.1	96	7.5YR 8/6	jbm+ca
A29	16 : 1 : 8	9.0	0	7.5YR 8/3	cfa
		6.7	96	7.5YR 6/6	jbm+ca
A30	5 : 1 : 7	10.1	0	7.5YR 8/3	cfa
		9.9	96	7.5YR 6/6	jbm
A31	4 : 1 : 8	10.4	0	7.5YR 8/3	cfa
		9.5	96	7.5YR 5/8	jbm
A32	10 : 1 : 14	10.6	0	7.5YR 8/3	cfa
		9.8	96	7.5YR 7/6	jbm
A33	8 : 1 : 16	10.6	0	7.5YR 8/3	cfa
		9.7	96	7.5YR 7/8	jbm
A34	2 : 3 : 3	8.3	0	7.5YR 6/8	cfa
		8.0	168	10YR 5/6	yuk
		7.9	336	10YR 5/6	yuk

		7.8	504	10YR 5/6	yuk
		7.9	672	10YR 5/6	yuk
		7.8	840	10YR 5/6	yuk
A35	8 : 3 : 4	9.5	0	7.5YR 6/6	cfa
		7.3	168	7.5YR 6/6	ca
		7.0	336	7.5YR 6/6	ca
		6.9	504	7.5YR 6/6	ca
		7.0	672	7.5YR 6/6	ca
		6.8	840	7.5YR 6/6	ca
A36	3 : 8 : 2	8.8	0	7.5YR 4/6	Fh
		7.8	168	7.5YR 4/6	Fh
		7.6	336	7.5YR 4/6	Fh+ca
		7.2	504	7.5YR 4/6	Fh+ca
		7.3	672	7.5YR 4/6	Fh+ca
		7.3	840	7.5YR 4/6	Fh+ca
A37	3 : 7 : 6	8.3	0	7.5YR 5/6	cfa
		8.4	168	10YR 4/6	cfa
		8.1	336	10YR 4/6	yuk
		8.0	504	10YR 4/6	yuk
		7.9	672	10YR 4/6	yuk
		7.9	840	10YR 4/6	yuk
A38	2 : 1 : 2	9.8	0	7.5YR 6/8	am
		9.1	168	7.5YR 6/8	jbm
		8.8	336	7.5YR 6/8	jbm
		8.6	504	7.5YR 6/8	jbm
		8.6	672	7.5YR 6/8	jbm
		8.4	840	7.5YR 6/8	jbm
A40	2 : 3 : 3	7.1	0		
		6.6	480	10YR 5/6	asd
A41	2 : 3 : 3	6.1	0		
		3.0	480	10YR 5/6	asd
A42	2 : 3 : 3	4.7	0		
		3.1	480	10YR 5/6	asd+sc
A43	1 : 1 : 1	6.0	0		
		3.3	288	10YR 5/6	asd
A44	1 : 1 : 1	5.0	0		
		4.3	288	10YR 6/8	sc+asd
A45	1 : 1 : 1	4.1	0		
		4.6	288	10YR 8/6	sc
K09	2 : 3 : 3	6.0	1	7.5YR 5/6	cfa
		4.9	13	10YR 4/4	yuk
		5.2	24	10YR 5/6	yuk
		4.7	37	10YR 5/6	asd
		5.1	49	10YR 5/6	asd
		4.6	61	10YR 5/6	asd
		4.3	73	10YR 5/6	asd
		4.1	94	10YR 5/6	asd
		4.0	168	10YR 5/6	asd

		4.0	286	10YR 5/6	asd
K10	2 : 3 : 3	7.1	1	7.5YR 5/6	cfa
		6.9	13	7.5YR 5/6	cfa
		6.8	24	7.5YR 5/6	yuk
		7.0	37	10YR 4/4	yuk
		7.3	49	10YR 4/4	yuk
		7.3	61	10YR 4/4	yuk
		7.3	73	10YR 5/6	yuk
		7.3	94	10YR 5/6	asd
		7.2	168	10YR 5/6	asd
		7.3	286	10YR 5/6	asd
K11	2 : 3 : 3	8.1	1	7.5YR 6/8	cfa
		7.7	13	7.5YR 5/6	cfa
		8.0	24	10YR 4/6	yuk
		8.1	37	10YR 4/6	yuk
		8.4	49	10YR 4/6	yuk
		8.3	61	10YR 4/6	yuk
		8.4	73	10YR 4/6	yuk
		8.3	94	10YR 4/6	yuk
		8.1	168	10YR 5/6	yuk
		8.0	286	10YR 5/6	asd
K12	2 : 3 : 3	9.0	1	7.5YR 6/6	cfa
		8.6	13	7.5YR 5/8	cfa
		8.8	24	7.5YR 5/8	yuk
		8.8	37	7.5YR 5/6	yuk
		8.8	49	7.5YR 5/6	yuk
		8.8	61	7.5YR 5/6	yuk
		8.9	73	7.5YR 5/6	yuk
		8.8	94	7.5YR 5/6	yuk
		8.6	168	7.5YR 5/6	yuk
		8.5	286	7.5YR 5/6	yuk
Continuous synthesis					
C03	2 : 3 : 3	4.5	480	10YR 5/6	asd
C04	2 : 3 : 3	8.6	480	7.5YR 5/6	yuk
C05	2 : 3 : 3	9.1	0	7.5YR 4/6	cfa
		9.2	12	7.5YR 5/6	cfa
		9.2	24	7.5YR 5/6	cfa
		9.2	36	7.5YR 5/6	cfa
		9.2	48	7.5YR 5/6	yuk
		9.2	60	7.5YR 5/6	yuk
		9.2	72	7.5YR 5/6	yuk
		9.2	96	7.5YR 5/6	yuk
		9.2	120	7.5YR 5/6	yuk
		9.2	144	7.5YR 5/6	yuk+ca
		9.2	168	7.5YR 5/6	yuk+ca
		9.2	216	7.5YR 5/6	yuk+ca
		9.2	264	7.5YR 5/6	yuk+ca
		9.2	312	7.5YR 5/6	yuk+ca

9.2	432	7.5YR 5/6	yuk+ca
9.2	552	7.5YR 5/6	yuk+ca
9.2	792	7.5YR 5/6	yuk+ca

color refers to Munsell color chart; asd: arseniosiderite; ca: Ca arsenate; cfa:amorphous calcium ferric arsenate; Fh: ferrihydrite; jbm: johnbaumite; yuk: yukonite.

Table 3. Compositions of the precipitates*

wt%	K10-1 cfa	K11-13 cfa	K12-1 cfa	K12-13 cfa	A34-0 cfa	A37-168 cfa	A35-0 cfa+ca	A36-0 Fh
Fe_2O_3	30.24	29.72	31.05	31.08	27.99	30.98	17.03	49.37
CaO	12.58	14.02	14.17	14.43	12.90	9.67	24.88	11.87
As_2O_5	37.97	33.20	34.56	33.14	34.24	31.52	32.85	16.45
SiO_2	0.36	0.68	0.47	0.59	0.55	4.09	0.49	0.57
Na_2O	0.88	1.23	1.48	1.74	2.54	4.49	1.89	0.16
formula								
Fe	3.0	3.0	3.0	3.0	3.0	3.0		
Ca	1.8	2.0	2.0	2.0	2.0	1.3		
AsO_4	2.6	2.3	2.3	2.2	2.6	2.1		
SiO_4	0.0	0.1	0.1	0.1	0.1	0.5		
OH	4.7	6.0	6.1	6.4	5.7	4.3		
H_2O	5.5	6.5	4.8	4.9	7.5	6.1		

*Bulk chemical compositions except for unknown Ca arsenate (ca); cfa: amorphous calcium ferric arsenate; ca: calcium arsenate; Fh: ferrihydrite; Mineral formula based on 17 O recast to 3 Fe for the amorphous Ca ferric arsenate, yukonite and arseniosiderite, and 10 O for Ca arsenate.

Table 3. cont.

wt%	K12-286 yuk	K09-73 asd	K11-286 asd	C03-480 asd	therm** asd	ca
Fe_2O_3	30.22±0.24	28.11	29.61	31.39±0.90	32.69	0.19±0.04
CaO	11.95±0.21	11.70	11.84	14.25±0.21	13.92	37.61±0.33
As_2O_5	32.89±0.35	38.51	32.30	42.59±0.90	43.04	51.85±0.40
SiO_2	5.13±0.29	0.48	5.48	0.74±0.04	na	na
Na_2O	2.43±0.03	2.68	2.35	0.44±0.02	na	0.60±0.07
H_2O	na	na	na	na	10.99	na
formula						
Fe	3.0	3.0	3.0	3.0	3.0	0.0
Ca	1.7	1.8	1.7	1.9	1.8	2.8
AsO_4	2.3	2.9	2.3	2.8	2.7	1.9
SiO_4	0.7	0.1	0.7	0.1		0.0
OH	3.5	4.4	3.3	4.1	4.4	
H_2O	5.9	6.6	6.7	2.4	2.0	2.3

** arseniosiderite used in calorimetry experiments.

Table 4. Local structural parameters of the Ca-Fe arsenate precipitates determined from As-EXAFS

		N	*R*	σ^2	*ΔE0*	*rf*	rX^2
K09-1	O	4.4±0.3	1.69±0.00	0.0030	6.8	0.014	124
pH 6; 1h	Fe	2*	3.32±0.03	0.0133			
	MS21	12*	3.08±0.04	0.0030[a]			
K09-24	O	4.3±0.3	1.69±0.00	0.0028	6.6	0.015	108
pH 6; 24h	Fe1	2*	3.21±0.02	0.0098			
	Fe2	1*	3.34±0.07	"			
	MS21	12*	3.15±0.06	0.0028[a]			
K09-286	O	4.4±0.3	1.70±0.00	0.0031	7.9	0.014	72
pH 6; 286h	Fe1	2*	3.21±0.02	0.0089			
	Fe2	1*	3.35±0.05	"			
	MS21	12*	3.16±0.07	0.0031[a]			
K10-1	O	4.1±0.2	1.70±0.00	0.0025	7.9	0.011	81
pH 7; 1h	Fe	2*	3.30±0.03	0.0151			
	MS21	12*	3.12±0.03	0.0025[a]			
K10-37	O	4.2±0.2	1.70±0.00	0.0029	8.3	0.010	78
pH 7; 37h	Fe1	2*	3.21±0.02	0.0091			
	Fe2	1*	3.35±0.04	"			
	MS21	12*	3.16±0.05	0.0029[a]			
K10-286	O	4.5±0.3	1.69±0.00	0.0032	7.0	0.016	112
pH 7; 286h	Fe1	2*	3.20±0.02	0.0083			
	Fe2	1*	3.35±0.05	"			
	MS21	12*	3.15±0.07	0.0032[a]			
K11-1	O	4.2±0.2	1.70±0.00	0.0024	7.7	0.011	76
pH 8; 1h	Fe	2*	3.29±0.04	0.0173			
	MS21	12*	3.13±0.03	0.0024[a]			
K11-49	O	4.4±0.3	1.69±0.00	0.0028	6.0	0.013	516
pH 8; 49h	Fe1	2*	3.19±0.02	0.0075			
	Fe2	1*	3.34±0.04	"			
	MS21	12*	3.16±0.06	0.0028[a]			
K11-286	O	4.4±0.3	1.69±0.00	0.0030	7.0	0.012	647
pH 8; 286h	Fe1	2*	3.21±0.01	0.0068			
	Fe2	1*	3.34±0.04	"			
	MS21	12*	3.18±0.07	0.0030[a]			

Fits performed in *R*-space (*R*=1-4 Å; *k*=3-15 $Å^{-1}$); amplitude reduction factor (S_0^2) is constrained to 1.0; *N*: coordination number; *R*: interatomic distance (Å); σ^2: Debye–Waller parameter ($Å^2$); *ΔE0*: energy offset (eV); *rf*: r-factor and rX^2 reduced chi square as the goodness-of-fit parameters; Multiple scattering paths MS21, refers to As-O1-O2; Number of independent points are 23 for all and number of variables are between 7 and 8; * Fixed value; [a] defined as $\sigma^2_{As\text{-}O}$

Table 5. Local structural parameters of the Ca-Fe arsenate precipitates determined from Fe-EXAFS

		N	*R*	σ^2	*ΔE0*	*rf*	rX^2
K09-1	O	6.0±0.3	1.99±0.00	0.0068	-1.5	0.0050	47
pH 6; 1h	Fe	1.5*	3.05±0.05	0.0218			
	As	2*	3.33±0.01	0.0101			
	Ca	0.5*	3.67±0.03	0.0036			
	DST	24*	3.35±0.09	0.0136[b]			
	DSC	6*	3.99±0.09	"			
	TSC	6*	3.99[a]	0.0274[c]			
K09-24	O	5.9±0.5	2.00±0.01	0.0080	-0.8	0.0180	132
pH 6; 24h	Fe1	1.5*	3.09±0.04	0.0120			
	As1	1*	3.26±0.08	0.0070			
	As2	1*	3.41±0.07	"			
	Fe2	1*	3.52±0.06	0.0120[d]			
K09-286	O	6.6±0.5	2.02±0.01	0.0075	-0.9	0.0111	169
pH 6; 286h	Fe1	2*	3.12±0.02	0.0074			
	As1	2*	3.26±0.03	0.0058			
	As2	2*	3.41±0.03	"			
	Fe2	2*	3.50±0.03	0.0074[d]			
K10-1	O	6.1±0.3	1.99±0.00	0.0072	-2.3	0.0050	47
pH 7; 1h	Fe	1.5*	3.03±0.02	0.0127			
	As	2*	3.34±0.02	0.0128			
	Ca	0.5*	3.67±0.03	0.0033			
	DST	24*	3.16±0.09	0.0143[b]			
	DSC	6*	3.92±0.12	"			
	TSC	6*	3.92[a]	0.0287[c]			
K10-37	O	5.8±0.7	2.00±0.01	0.0075	-2.1	0.0259	336
pH 7; 37h	Fe1	1.5*	3.05±0.03	0.0075			
	As1	1.5*	3.18±0.06	0.0082			
	As2	2*	3.37±0.03	"			
	Fe2	1*	3.52±0.05	0.0075[d]			
K10-286	O	6.5±0.5	2.02±0.01	0.0082	-0.8	0.0105	88
pH 7; 286h	Fe1	2*	3.13±0.02	0.0099			
	As1	2*	3.28±0.02	0.0046			
	As2	2*	3.43±0.02	"			
	Fe2	2*	3.53±0.02	0.0099[d]			
K11-1	O	5.8±0.4	1.99±0.00	0.0082	-1.1	0.0060	126
pH 8; 1h	Fe	1.5*	3.04±0.02	0.0142			
	As	2*	3.35±0.02	0.0122			
	Ca	0.5*	3.67±0.06	0.0078			
	DST	24*	3.32±0.09	0.0164[b]			
	DSC	6*	3.98±0.11	"			
	TSC	6*	3.98[a]	0.0327[c]			
K11-49	O	6.2±0.4	2.01±0.01	0.0075	-0.5	0.0085	80
pH 8; 49h	Fe1	2*	3.08±0.01	0.0078			
	As1	1.5*	3.23±0.02	0.0056			
	As2	2*	3.42±0.02	"			
	Fe2	1*	3.49±0.06	0.0078[d]			

K11-286	O	6.8±0.7	2.01±0.01	0.0091	-2.1	0.0189	84
pH 8; 286h	Fe1	2*	3.08±0.02	0.0081			
	As1	2*	3.22±0.03	0.0057			
	As2	2*	3.38±0.03	"			
	Fe2	2*	3.51±0.02	0.0081[d]			
C03-480	O	6.4±0.5	2.02±0.01	0.0073	-0.5	0.0098	153
pH 4.5; 480h	Fe1	2*	3.12±0.02	0.0080			
	As1	2*	3.27±0.02	0.0050			
	As2	2*	3.42±0.02	"			
	Fe2	2*	3.51±0.02	0.0080[d]			

Fits performed in *R*-space (*R*=1-4 Å; *k*=2.5-14 $Å^{-1}$); amplitude reduction factor (S_0^2) is constrained to 0.8; *N*: coordination number; *R*: interatomic distance (Å); σ^2: Debye–Waller parameter ($Å^2$); $\Delta E0$: energy offset (eV); *rf*: r-factor and rX^2 reduced chi square as the goodness-of-fit parameters; Multiple scattering paths DST, DSC and TSC refer to Fe-O1-O2 (triangular), Fe-O1-O3 (collinear) and Fe-O1-Fe-O1 respectively; Number of independent points are 21.7 for all and number of variables are between 10 and 12; * Fixed value; [a] constrained to R_{DSC} ; [b] defined as $2x\sigma^2_{Fe\text{-}O}$; [c] defined as $4x\sigma^2_{Fe\text{-}O}$; [d] constrained as $\sigma^2_{Fe\text{-}Fe1}$

Table 6. Thermochemical cycle for arseniosiderite. All reactants and products are at T = 298.15 K. All enthalpy values in kJ mol^{-1}.

Reaction and reaction number	
$Ca(OH)_2$ (cr) + $2H^+$(aq) = Ca^{2+}(aq) + $2H_2O$ (aq)	1
γ-FeOOH·$0.162H_2O$ (cr) + $3H^+$(aq) = Fe^{3+}(aq) + $2.162H_2O$ (aq)	2
KH_2AsO_4 (cr) = K^+(aq) + $2H^+$(aq) + AsO_4^{3-}(aq)	3
HCl·$9.96H_2O$ (l) = H^+(aq) + Cl^-(aq) + $9.96H_2O$ (aq)	4
H_2O (l) = H_2O (aq)	5
KCl (cr) = K+(aq) + Cl^-(aq)	6
γ-FeOOH·$0.162H_2O$ (cr) = γ-FeOOH (cr) + $0.162H_2O$ (l)	7
$Ca_{0.663}Fe_{1.093}(AsO_4)(OH)_{1.605}$·$0.827H_2O$ (cr) + $1.605H^+$ (aq) = $0.663Ca^{2+}$ (aq) + $1.093Fe^{3+}$ (aq) + AsO_4^{-3} (aq) + $2.432H_2O$ (aq)	8
$0.663Ca(OH)_2$ (cr) + 1.093γ-FeOOH (cr) + KH_2AsO_4 (cr) + HCl·$9.96H_2O$ (l) = $11.04H_2O$ (l) + KCl (cr) + $Ca_{0.663}Fe_{1.093}(AsO_4)(OH)_{1.605}$·$0.827H_2O$ (cr)	9
$10.46H_2$ (g) + $4.98O_2$ (g) + $1/2Cl_2$ (g) = HCl·$9.96H_2O$ (l)	10
Fe (cr) + O_2 (g) + $1/2H_2$ (g) = γ-FeOOH (cr)	11
K (cr) + H_2 (g) + As (cr) + $2O_2$ (g) = KH_2AsO_4 (cr)	12
H_2 (g) + $1/2O_2$ (g) = H_2O (l)	13
K (cr) + $1/2Cl_2$ (g) = KCl (cr)	14
Ca (cr) + O_2 (g) + H_2 (g) = $Ca(OH)_2$ (cr)	15
$0.663Ca$ (cr) + 1.093Fe (cr) + As (cr) + $3.216O_2$ (g) + $1.6295H_2$ (g) = $Ca_{0.663}Fe_{1.093}(AsO_4)(OH)_{1.605}$·$0.827H_2O$ (cr)	16

enthalpy value	reference
$\Delta H_1 = -133.52^a \pm 0.68^b (2)^c$	this work
$\Delta H_2 = -46.62 \pm 0.13(12)$	Majzlan (2011)
$\Delta H_3 = +24.97 \pm 0.14(5)$	Majzlan (2011)
$\Delta H_4 = 0$	enthalpy of dissolution of HCl·$9.96H_2O$ in HCl·$9.96H_2O$
$\Delta H_5 = -0.54$	calculated from Parker (1965)
$\Delta H_6 = +17.78 \pm 0.11(11)$	Majzlan (2011), with additional data from this work
$\Delta H_7 = +1.41 \pm 0.17$	calculated from Majzlan et al. (2007)
$\Delta H_8 = -29.24 \pm 0.16(5)$	this work
$\Delta H_9 = 0.663\Delta H_1 + 1.093\Delta H_2 + \Delta H_3 + \Delta H_4 - 11.04\Delta H_5 - \Delta H_6 - \Delta H_8 - 1.093\Delta H_7 = -98.64 \pm 0.54$	
$\Delta H_{10} = -3007.9 \pm 1.0$	calculated from NBS 270-3
$\Delta H_{11} = -549.4 \pm 1.4$	Majzlan et al. (2003)
$\Delta H_{12} = -1181.2 \pm 2.0$	see Majzlan (2011) for the derivation of this value
$\Delta H_{13} = -285.8 \pm 0.1$	Robie and Hemingway (1995)
$\Delta H_{14} = -436.5 \pm 0.1$	Robie and Hemingway (1995)
$\Delta H_{15} = -986.1 \pm 1.3$	Robie and Hemingway (1995)
$\Delta H_{16} = \Delta H_9 + 0.663\Delta H_{15} + 1.093\Delta H_{11} + \Delta H_{12} + \Delta H_{10} - 11.04\Delta H_{13} - \Delta H_{14}$	
$\Delta H_{16} = \Delta_f H^o$(arseniosiderite) = -1950.3 ± 3.1	

[a] mean
[b] two standard deviations of the mean
[c] number of measurements

Table 7. Thermodynamic functions for arseniosiderite.

T K	C_p J mol^{-1} K^{-1}	H_T-H_0 kJ mol^{-1}	S J mol^{-1} K^{-1}	G_T-G_0 kJ mol^{-1}
0	0	0	0*	0
25	11.51	98.07	5.866	-48.58
60	51.29	1162	29.95	-635.1
100	97.95	4170	67.34	-2564
150	144.0	10350	116.8	-7170
200	169.7	18200	161.8	-14160
250	191.1	27220	202.0	-23270
300	213.6	37320	238.7	-34300

*Nominal value (see text). Refer to Table S2 for the complete data.

Table 8. Auxiliary data used for the calculation of formation entropy, formation Gibbs free energy and solubility product. All entropy data from Robie and Hemingway (1995).

	S^o (J mol^{-1} K^{-1})		$\Delta_f G^o$ (kJ mol^{-1})	
Ca (cr)	42.9±0.1	H^+ (aq)	0	
Fe (cr)	27.09±0.13	Ca^{2+} (aq)	–553.6±1.0	Robie and Hemingway (1995)
As (cr)	35.69±0.84	Fe^{3+} (aq)	–16.7±2.0	Robie and Hemingway (1995)
O_2 (g)	205.15±0.02	AsO_4^{3-} (aq)	–647.618±1.5	Nordstrom et al. (2014)
H_2 (g)	130.68±0.02	H_2O (l)	–237.14±0.04	Nordstrom and Munoz (1994)

Table 9. Summary of the thermodynamic data for arseniosiderite. The enthalpy of dissolution ($\Delta_{diss}H$) refers to dissolution in 5 *N* HCl at *T* = 298.15 K. $\Delta_r H^o$, $\Delta_r G^o$ and logK_{sp} values refer to reaction $Ca_{0.663}Fe_{1.093}(AsO_4)(OH)_{1.605}\cdot 0.827H_2O$ (cr) + 1.605H^+ (aq) = 0.663Ca^{2+} (aq) + 1.093Fe^{3+} (aq) + AsO_4^{3-} (aq) + 2.432H_2O (aq). The values are on purpose listed to more decimal places than justified by the uncertainties, to avoid round-off errors when entering them into thermodynamic databases.

M_r (g mol^{-1})	268.7229
$\Delta_{diss}H$ (kJ mol^{-1})	–29.24±0.16
$\Delta_f H^o$ (kJ mol^{-1})	–1950.27±3.10
S^o (J mol^{-1} K^{-1})	237.43±4.37
$\Delta_f S^o$ (J mol^{-1} K^{-1})	–729.02±4.45
$\Delta_f G^o$ (kJ mol^{-1})	–1732.91±3.38
$\Delta_r H^o$ (kJ mol^{-1})	–51.48±6.50[a]
$\Delta_r G^o$ (kJ mol^{-1})	123.28±4.34[a]
logK_{sp}	–21.60±0.76[a]

Table 10. Electron microprobe analyses across the transition zone

	L1 scorodite			L2 yukonite			L4 arseniosiderite		
wt%	1	2	3	1	2	3	1	2	3
Fe_2O_3	34.61	34.55	33.49	21.82	20.73	22.74	18.67	17.92	19.83
CaO	1.30	1.16	0.80	8.91	8.57	9.24	8.70	8.36	9.30
As_2O_5	45.05	45.22	45.58	29.37	27.96	29.44	23.36	23.66	26.4
SiO_2	0.08	0.06	0.03	0.30	0.32	0.43	0.59	0.44	0.39
SO_3	1.84	1.82	1.32	0.06	0.08	0.05	0.41	0.31	0.03
Formula									
Fe	1.0	1.0	1.0	3.0	3.0	3.0	3.0	3.0	3.0
Ca	0.1	0.0	0.0	1.7	1.8	1.7	2.0	2.0	2.0
AsO_4	0.9	0.9	0.9	2.8	2.8	2.7	2.6	2.8	2.8
SiO_4	0.0	0.0	0.0	0.1	0.1	0.1	0.1	0.1	0.1

Mineral formula based on 17 O recast to 3 Fe for yukonite and arseniosiderite, and 6 O recast to 1 Fe for scorodite; low analytical totals are related to contribution of impregnated epoxy within the porosity of the nanocrystalline Ca-Fe arsenate aggregates.

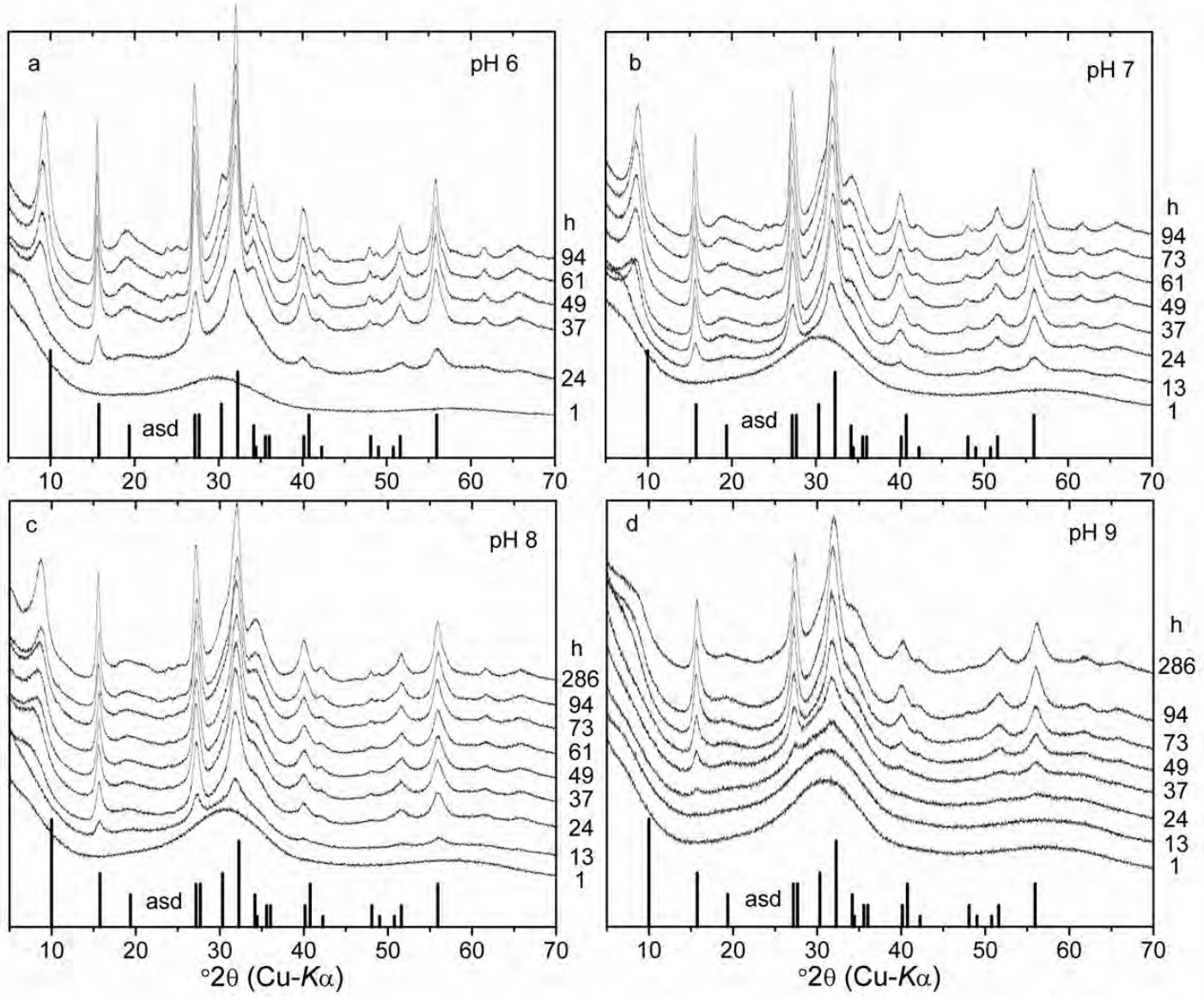
a
pH 6
h
94
61
49
37
24
1
asd
b
pH 7
h
94
73
61
49
37
24
13
1
asd
c
pH 8
h
286
94
73
61
49
37
24
13
1
asd
d
pH 9
h
286
94
73
49
37
24
13
1
asd
10 20 30 40 50 60 70
°2θ (Cu-Kα)

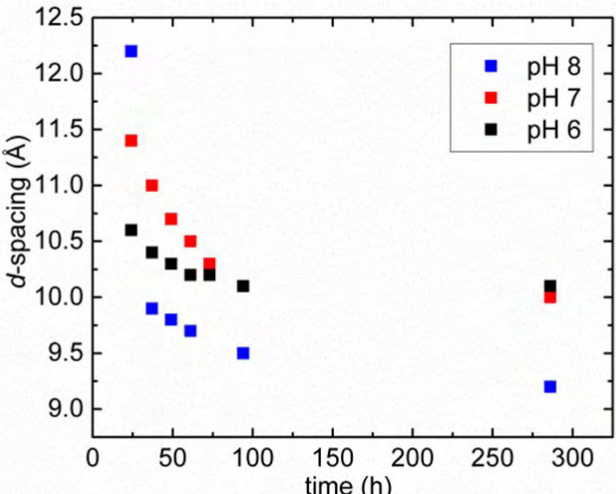
12.5
12.0
11.5
11.0
10.5
10.0
9.5
9.0
d-spacing (Å)
0
50
100
150
200
250
300
time (h)
pH 8
pH 7
pH 6

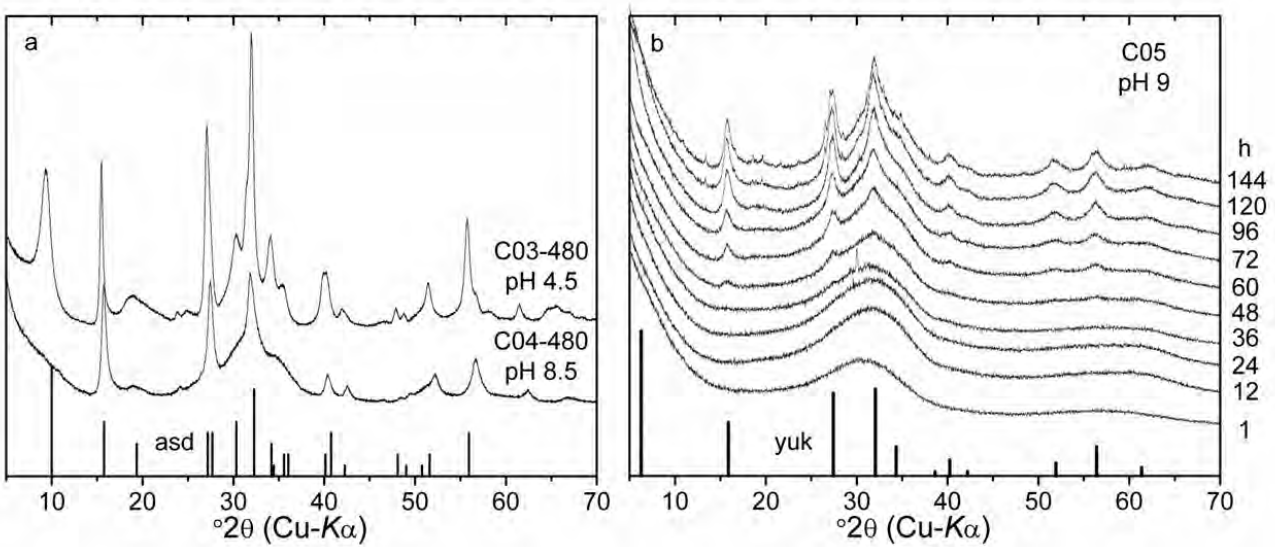
a
C03-480
pH 4.5
C04-480
pH 8.5
asd
10
20
30
40
50
60
70
°2θ (Cu-Kα)
b
C05
pH 9
h
144
120
96
72
60
48
36
24
12
1
yuk
10
20
30
40
50
60
70
°2θ (Cu-Kα)

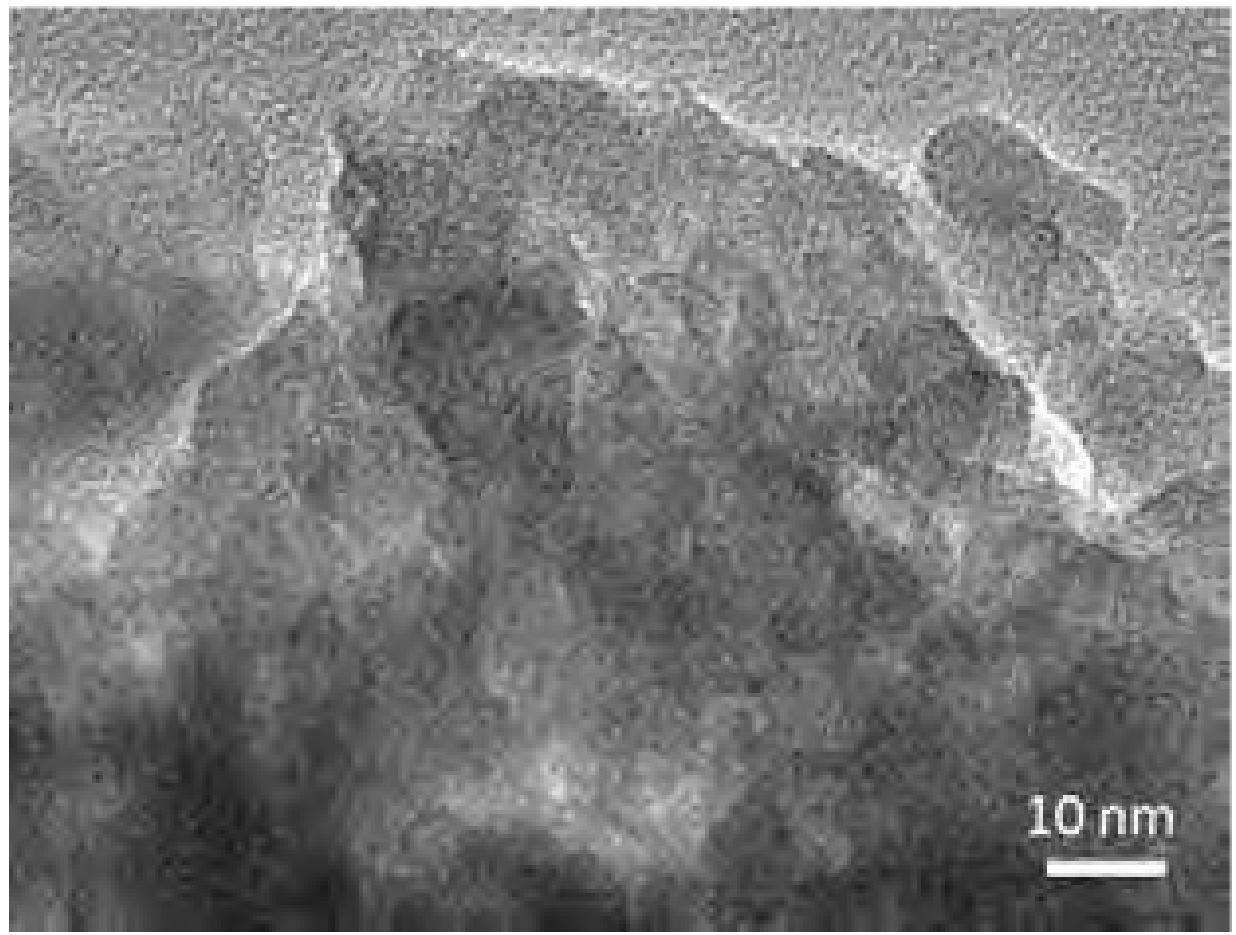
10 nm

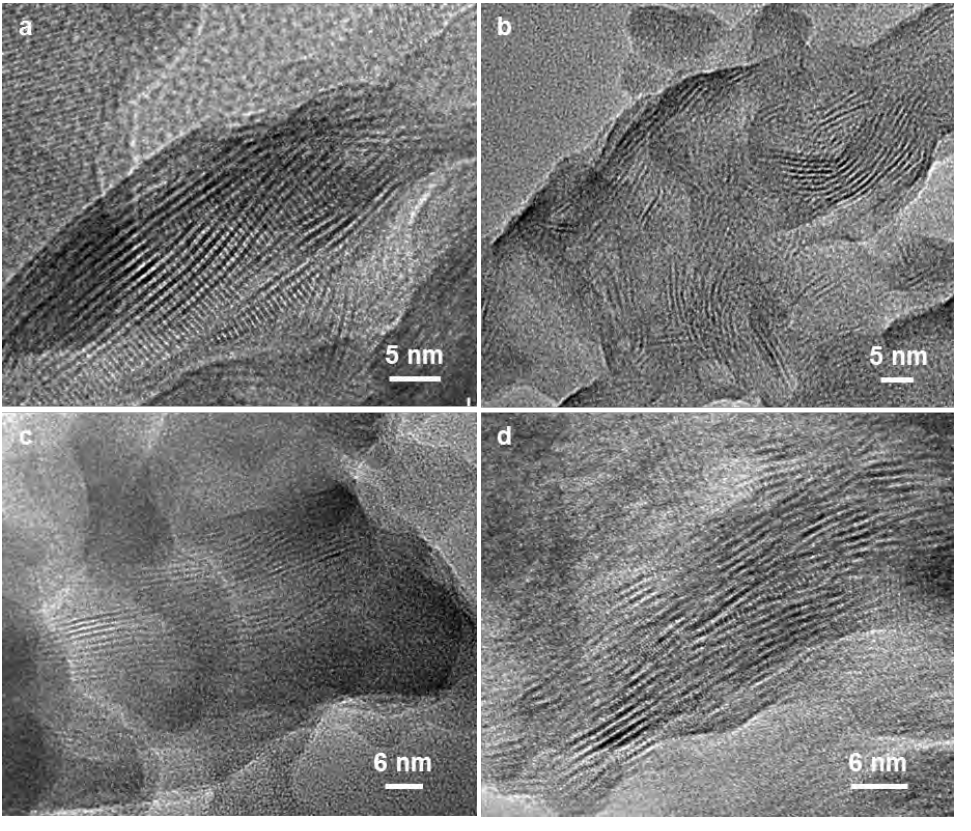
a
5 nm
b
5 nm
c
6 nm
d
6 nm

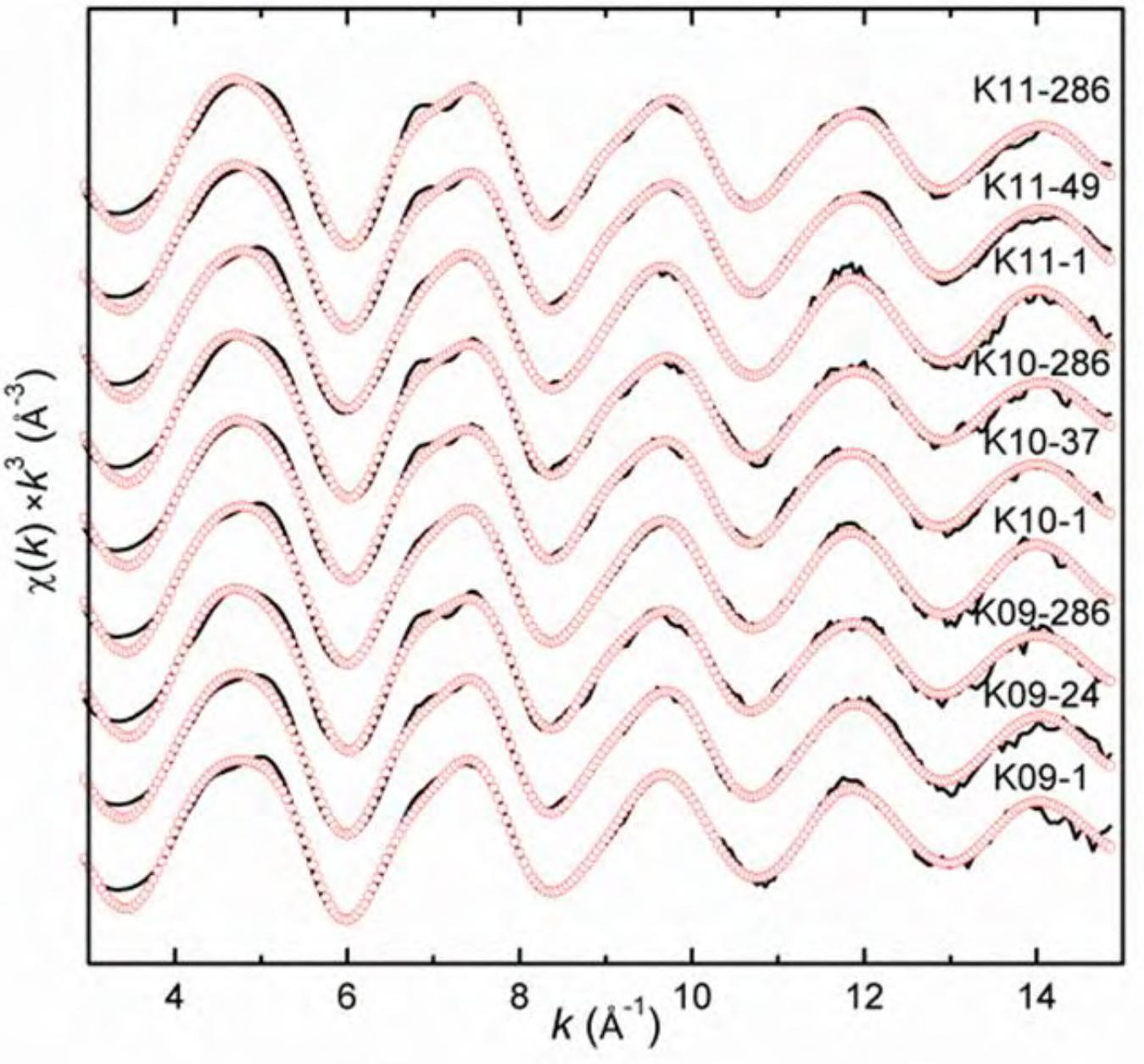
K11-286
K11-49
K11-1
K10-286
K10-37
K10-1
K09-286
K09-24
K09-1
χ(k) ×k³ (Å⁻³)
4
6
8
10
12
14
k (Å⁻¹)

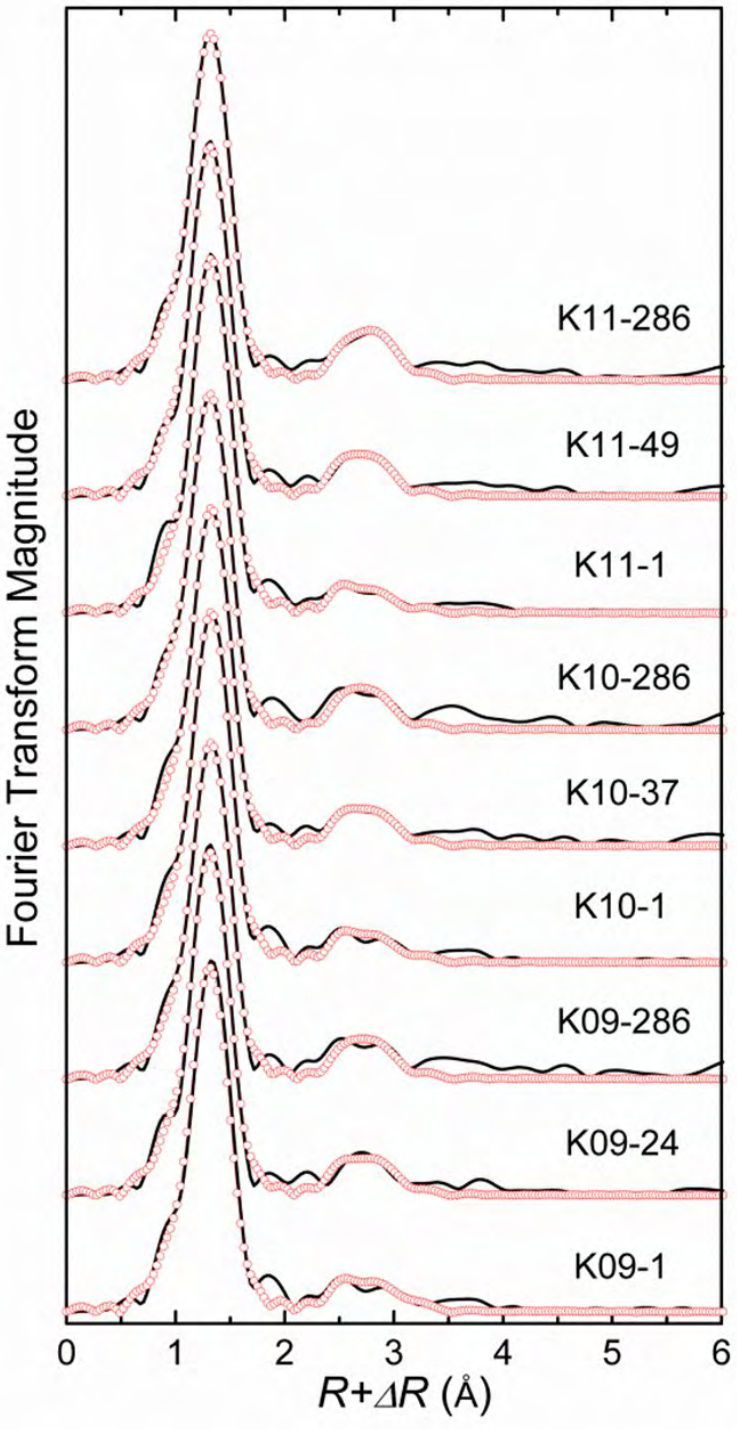
K11-286
K11-49
K11-1
K10-286
K10-37
K10-1
K09-286
K09-24
K09-1
Fourier Transform Magnitude
0
1
2
3
4
5
6
R+ΔR (Å)

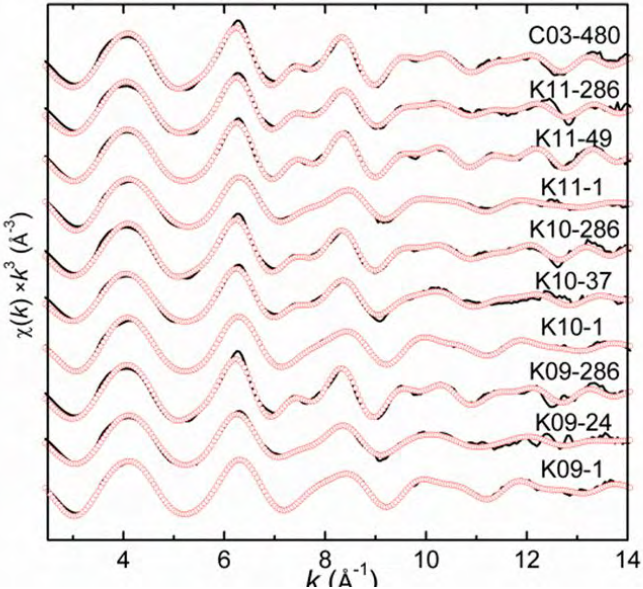
C03-480
K11-286
K11-49
K11-1
K10-286
K10-37
K10-1
K09-286
K09-24
K09-1
χ(k) ×k³ (Å⁻³)
4
6
8
10
12
14
k (Å⁻¹)

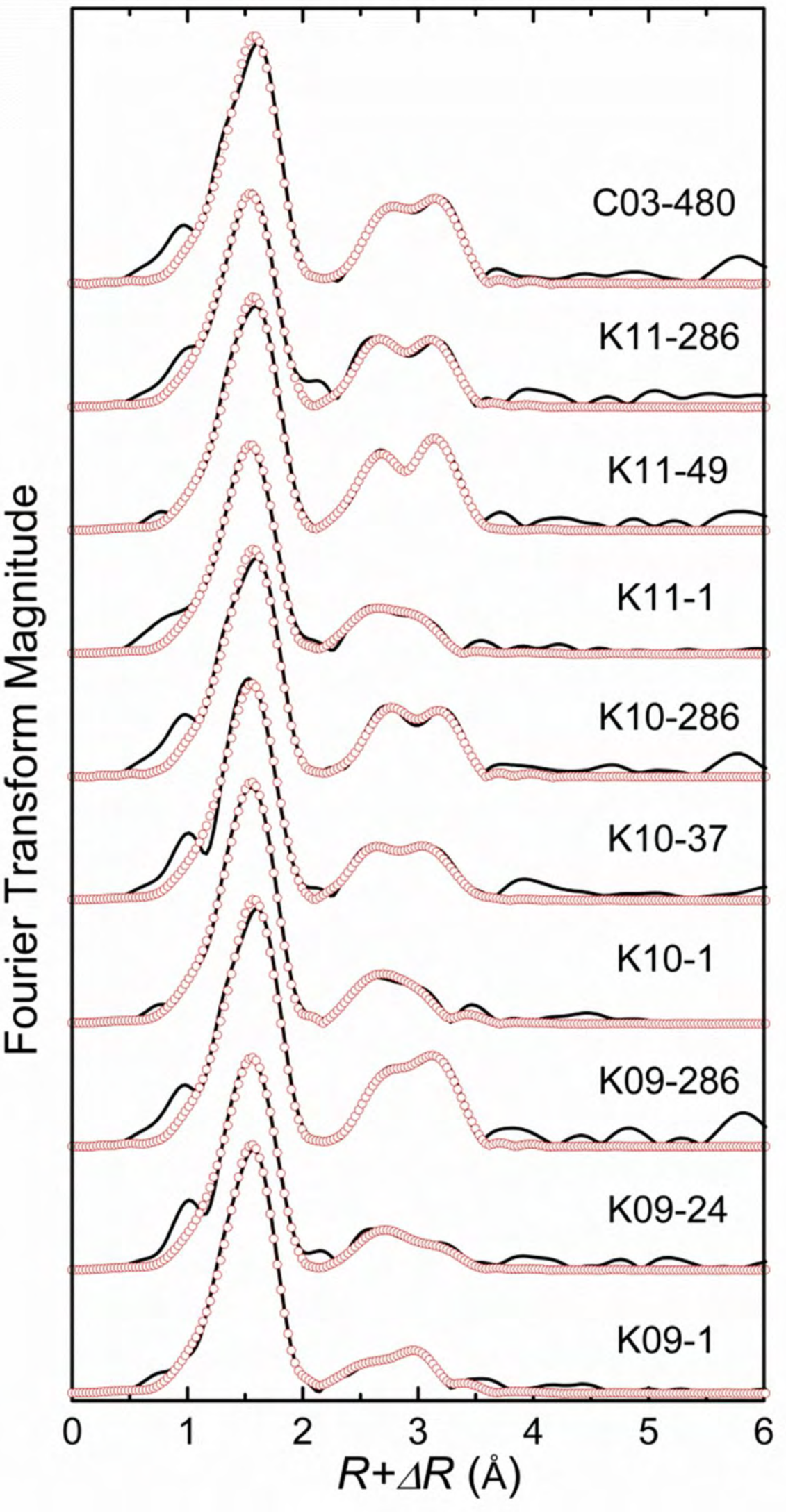
C03-480
K11-286
K11-49
K11-1
K10-286
K10-37
K10-1
K09-286
K09-24
K09-1
Fourier Transform Magnitude
0
1
2
3
4
5
6
R+ΔR (Å)

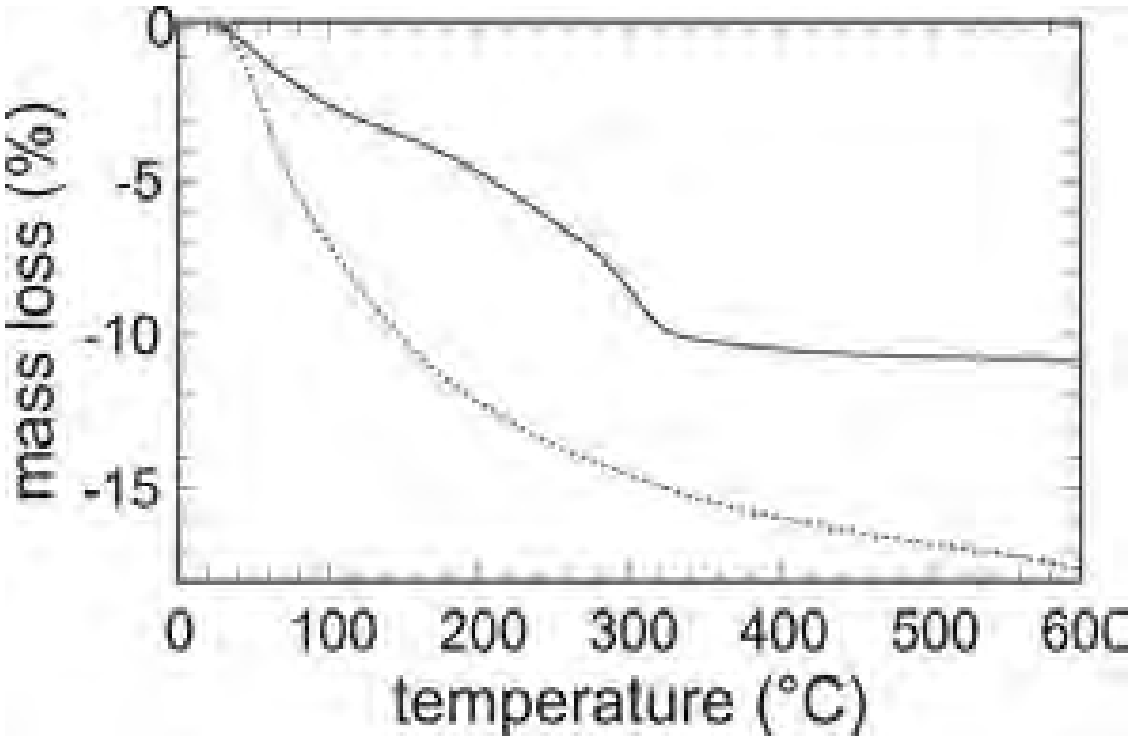
0
-5
-10
-15
mass loss (%)
0
100
200
300
400
500
600
temperature (°C)

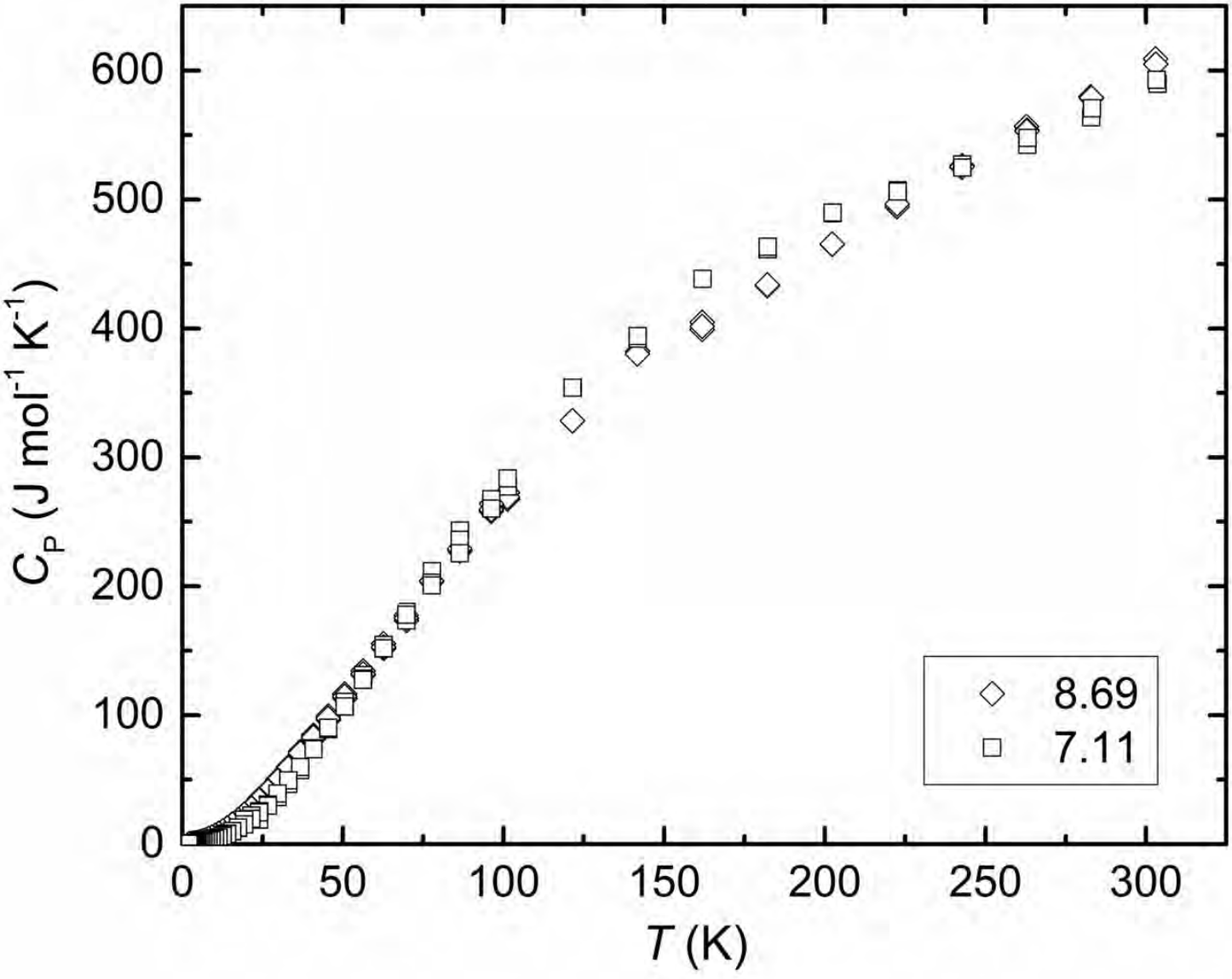
600
500
400
300
200
100
0
C_P (J mol^{-1} K^{-1})
0
50
100
150
200
250
300
T (K)
8.69
7.11

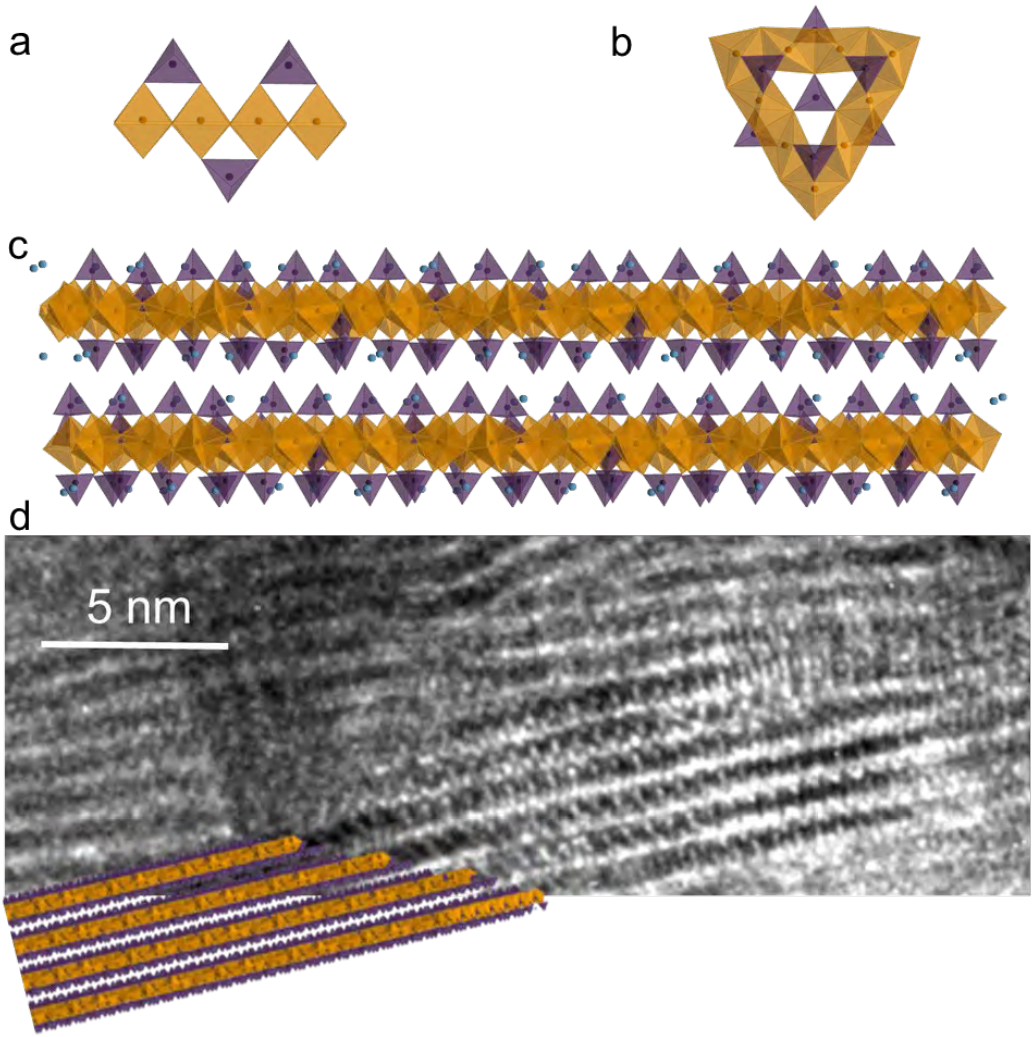
a
b
c
d
5 nm

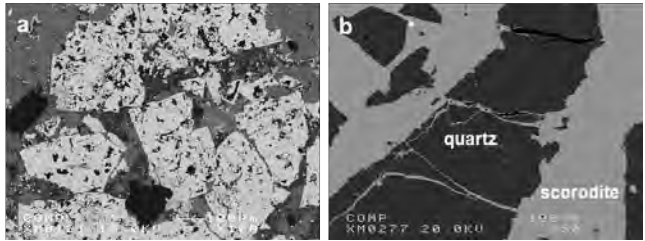
a
b
quartz
scorodite
COMP
XM0277 20.0KV

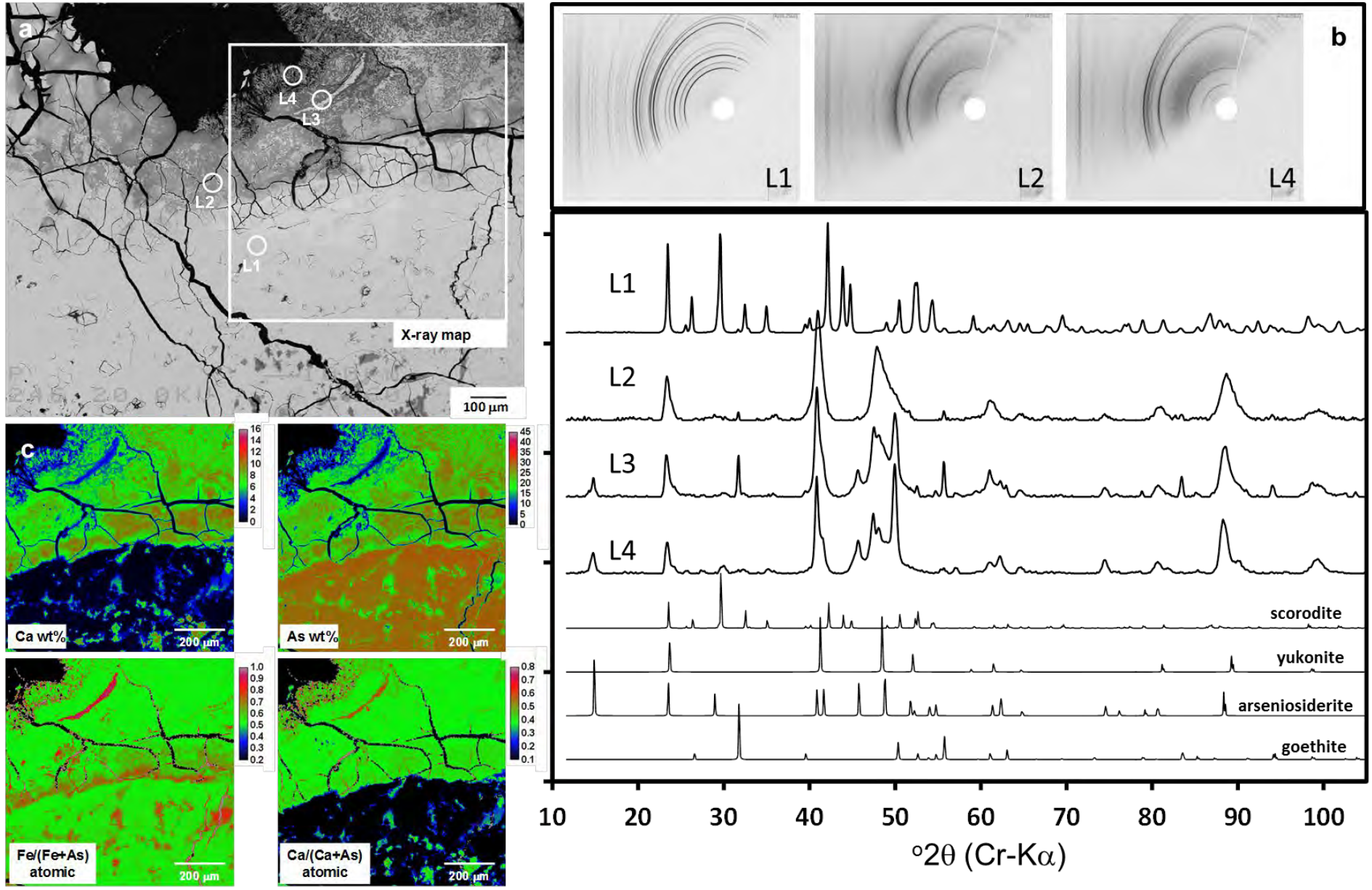
a
L4
L3
L2
L1
X-ray map
100 µm
b
L1
L2
L4
L1
L2
L3
L4
scorodite
yukonite
arseniosiderite
goethite
10
20
30
40
50
60
70
80
90
100
°2θ (Cr-Kα)
c
Ca wt%
200 µm
As wt%
200 µm
Fe/(Fe+As) atomic
200 µm
Ca/(Ca+As) atomic
200 µm

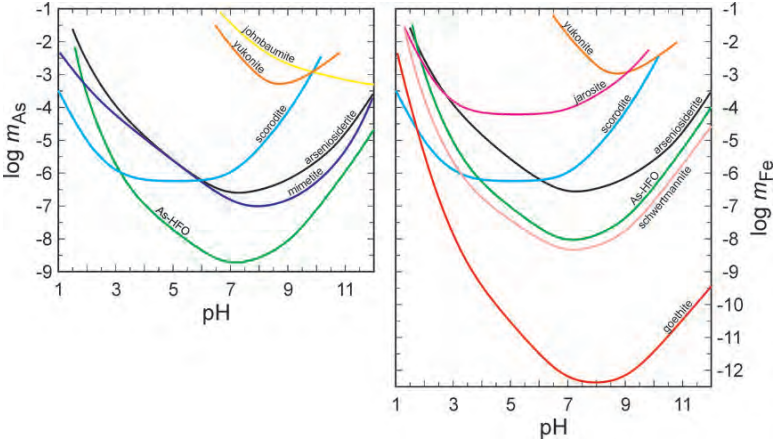
log m_{As}
pH
johnbaumite
yukonite
scorodite
arsenbosiderite
mimetite
As-HFO
log m_{Fe}
pH
yukonite
jarosite
scorodite
arsenbosiderite
As-HFO
schwertmannite
goethite

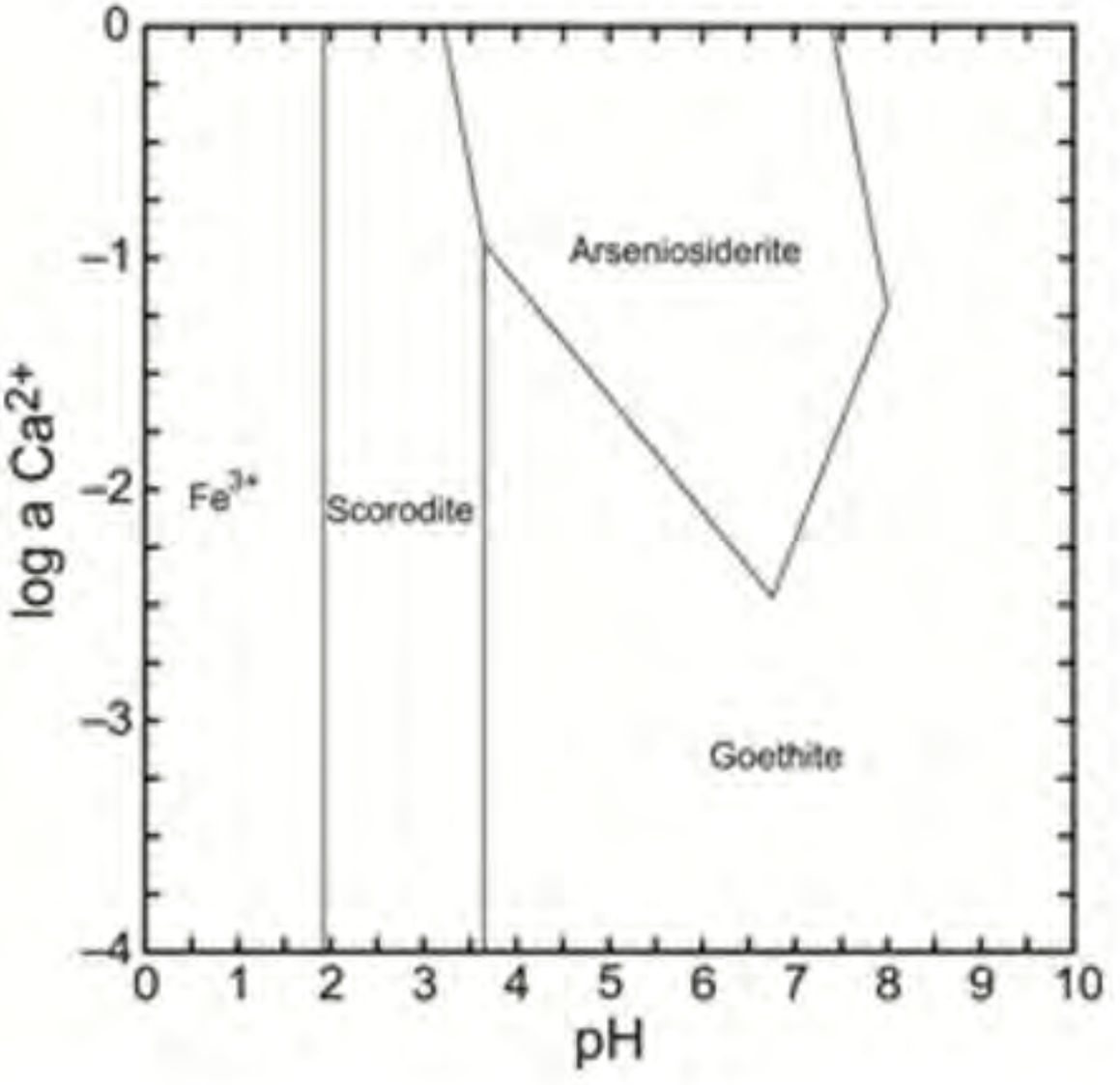
0
−1
−2
−3
−4
log a Ca2+
Fe3+
Scorodite
Arseniosiderite
Goethite
0 1 2 3 4 5 6 7 8 9 10
pH

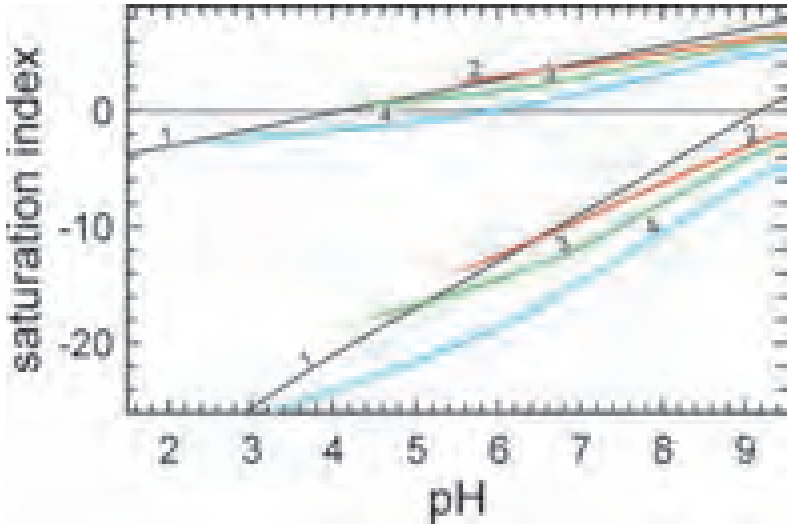
saturation index
0
-10
-20
2
3
4
5
6
7
8
9
pH